

# A model of force balance in Saturn’s magnetodisc

N. Achilleos<sup>1,2\*</sup>, P. Guio<sup>1,2</sup> and C. S. Arridge<sup>3,2</sup>

<sup>1</sup>*Department of Physics and Astronomy, University College London, Gower St., London, WC1E 6BT, U.K.*

<sup>2</sup>*The Centre for Planetary Sciences at UCL/Birkbeck, Gower St., London, WC1E 6BT, U.K.*

<sup>3</sup>*Mullard Space Science Laboratory, Department of Space and Climate Physics, UCL, Holmbury St. Mary, Dorking, Surrey, RH5 6NT, U.K.*

Date: 2009/09/08 15:23:59 , Revision: 1.97

## ABSTRACT

We present calculations of magnetic potential functions associated with the perturbation of Saturn’s planetary magnetic field by a rotating, equatorially-situated disc of plasma. Such structures are central to the dynamics of the rapidly rotating magnetospheres of Saturn and Jupiter. They are ‘fed’ internally by sources of plasma from moons such as Enceladus (Saturn) and Io (Jupiter). For these models, we use a scaled form of Caudal’s Euler potentials for the Jovian magnetodisc field (Caudal 1986). In this formalism, the magnetic field is assumed to be azimuthally symmetric about the planet’s axis of rotation, and plasma temperature is constant along a field line. We perturb the dipole potential (‘homogeneous’ solution) by using simplified distributions of plasma pressure and angular velocity for both planets, based on observations by the *Cassini* (Saturn) and *Voyager* (Jupiter) spacecraft. Our results quantify the degree of radial ‘stretching’ exerted on the dipolar field lines through the plasma’s rotational motion and pressure. A simplified version of the field model, the ‘homogeneous disc’, can be used to easily estimate the distance of transition in the outer magnetosphere between pressure-dominated and centrifugally-dominated disc structure. We comment on the degree of equatorial confinement as represented by the scale height associated with disc ions of varying mass and temperature. For the case of Saturn, we identify the principal forces which contribute to the magnetodisc current and make comparisons between the field structure predicted by the model and magnetic field measurements from the *Cassini* spacecraft. For the case of Jupiter, we reproduce Caudal’s original calculation in order to validate our model implementation. We also show that compared to Saturn, where plasma pressure gradient is, on average, weaker than centrifugal force, the outer plasmadisc of Jupiter is clearly a pressure-dominated structure.

**Key words:** (magnetohydrodynamics) MHD — plasmas — methods: numerical — planets and satellites: general

## 1 INTRODUCTION

Jupiter and Saturn are not only the largest planets in our Solar system, they are also the most rapid rotators. Gledhill (1967) first pointed out the important consequences of these properties for Jupiter’s magnetosphere. The rotational period of the planet is approximately 10 h, and as a result the gravitational ( $F_g$ ) and centrifugal ( $F_c$ ) forces associated with corotating plasma in Jupiter’s magnetosphere are equal at an equatorial distance of  $\sim 2.3 R_J$  from the planet’s centre (here, we denote Jupiter’s radius as  $R_J \approx 71000$  km). At the orbit of Io, situated at  $6 R_J$ , centrifugal force exceeds gravitational by a factor of nearly 20. Saturn’s radius ( $R_S \approx 60000$  km) and rotational period ( $\sim 10.75$  h) modify these distances to  $1.7 R_S$  ( $F_g = F_c$ ) and  $4.7 R_S$  ( $F_g \approx F_c/20$ ), the latter being  $0.7 R_S$  outside the orbital radius of the icy moon Enceladus.

Evidently, centrifugal force is an important factor for determining the structure of the outer magnetospheres of these planets.

Gledhill (1967) showed that the action of centrifugal force in Jupiter’s rapidly-rotating magnetosphere tends to confine magnetospheric plasma towards the equatorial plane, where the planet’s assumed dipolar field lines reach their maximum radial distances. A disc-like magnetospheric structure was thus anticipated, and indeed observed by the first spacecraft to visit the Jovian system, Pioneers 10 and 11 (Smith et al. 1974, 1975). The near-equatorial magnetic field structure seen by these spacecraft was very different from that of a rotating dipole throughout the region referred to as the middle magnetosphere, situated at distances  $\sim 20$ – $50 R_J$ . The magnetometer observations in this region showed a periodic pattern of largely radial field direction alternating with intervals having a north-south (meridionally-directed) field. These data were interpreted as periodic encounters with a rotating, disc-like current sheet. The highly radial field in this picture is a signature of magnetic field lines resembling a dipole pattern that has been radi-

\* E-mail: nick@apl.ucl.ac.uk

ally ‘stretched’ outwards near the magnetic equatorial plane. Such a magnetic geometry would be associated with an inward Lorentz force  $\sim \mathbf{J}_\phi \times \mathbf{B}$ , part of which is required to provide the centripetal acceleration for the rotating magnetospheric plasma (here  $\mathbf{J}_\phi$  denotes azimuthal current density and  $\mathbf{B}$  magnetic field).

Observations by *Galileo* (Kivelson et al. 1997) confirmed the persistence of this magnetodisc structure, and examined its response to changing solar wind conditions. During the late inbound pass of the *Galileo* insertion orbit, the magnetic field measurements indicated that a strong compression of the magnetosphere had taken place (Kivelson et al. 1997). This compression witnessed by *Galileo* resulted in an increase of the meridional field  $B_\theta$  by a factor of  $\sim 2$  when compared with the data from the Pioneer 10 outbound segment over the middle magnetospheric region at 30–50  $R_J$ . Like *Galileo*, Pioneer 10 outbound was a near-equatorial swathe situated at a local time near dawn. Unlike *Galileo*, however, the Pioneer 10 observations, acquired 22 years earlier, indicated a relatively quiescent magnetosphere. The conclusion was that the magnetospheric compression at the time of the *Galileo* insertion had caused an increase in meridional field  $B_\theta$  by squeezing the magnetic flux threading the magnetospheric plasma into a smaller volume (the change in location of the dawn magnetopause was inferred to be 40  $R_J$  inward). In addition, the periodic field signatures in meridional and radial field ( $B_\theta$  and  $B_r$ ) seen by *Galileo* indicated a thicker plasma sheet within the magnetodisc structure, as one would expect for a strongly-compressed magnetosphere.

The analogous behaviour for the magnetodisc at Saturn was explored by Arridge et al. (2008b), who took advantage of many orbits of magnetometer measurements from the *Cassini* spacecraft in order to investigate the relationship between magnetosphere size (as represented by the subsolar magnetopause standoff distance  $R_{MP}$ ) and the degree to which the radial field  $B_r$  dominated the field measurements seen in the outer magnetosphere. For the observations considered in this study, *Cassini* was typically situated on near-equatorial orbits just outside, and south of, the current sheet. This analysis revealed that, under conditions of low solar wind dynamic pressure (corresponding to  $R_{MP} > 23 R_S$ ), the magnetic field due to Saturn’s ring current (i.e. azimuthal current) dominates the planetary internal field in the outer magnetosphere, with the combination of the two producing the magnetodisc structure. For a more compressed magnetosphere, however, the dayside field became strongly dipolar, with magnetodisc geometry surviving only on the magnetosphere’s nightside and flanks. The Kronian magnetodisc may thus essentially disappear on the dayside under appropriate conditions, and is therefore even more sensitive than Jupiter’s magnetodisc in response to upstream solar wind conditions (Arridge et al. 2008b).

Connerney et al. (1981, 1983) provided the first detailed modelling of the ring current which supports the magnetodisc field at Saturn, and applied this model to the magnetometer data from the *Voyager* spacecraft encounters. The magnetic field in the Connerney, or CAN, model is computed by assuming, *a priori*, an azimuthally symmetric distribution of current which is confined to an annular disc of uniform thickness, extending between inner and outer edges at specified radial distances. Current density  $J_\phi$  in this model is assumed to be inversely proportional to radial distance ( $J_\phi \propto 1/r$ ). This formalism has been employed in several studies of the structure of Saturn’s ring current, usually based on fitting *in situ* magnetic field measurements from spacecraft (e.g. Connerney et al. (1983); Giampieri & Dougherty (2004); Bunce et al. (2007)).

The study by Bunce et al. (2007) emphasised that the current

which flows in the magnetodisc current sheet is a macroscopic manifestation of the microscopic drift motions of charged particles in the plasma. These authors examined the contribution of two types of azimuthal particle drift to the magnetic moment of the ring current: (i) The magnetic gradient drift exhibited by particles of finite thermal energy whose guiding centre moves in response to changes in field strength experienced during individual gyrations; (ii) The inertial drift associated with the centrifugal force in a frame which corotates with the local plasma flow. They showed that, for typical magnetospheric conditions at Saturn, the heavier (water-group) ions may generate a much stronger inertial current at distances beyond  $\sim 10 R_S$  due to their rotational kinetic energy exceeding typical thermal energy.

Empirical magnetic field models for the ring current at Jupiter and Saturn proposed by various authors (e.g. Gleeson & Axford (1976); Goertz et al. (1976); Connerney et al. (1981, 1983)) have proved to be valuable tools for determining the global length scales and intensity of the current which supports the magnetodisc field structure. Caudal (1986) pointed out that the *a priori* current distributions used in such models cannot be used to infer, unambiguously, the dynamical properties of the plasma in which the current flows. In particular, determining the relative importance of the plasma pressure gradient and centrifugal forces in generating the plasma current and magnetodisc field, requires a different approach which incorporates a knowledge of the plasma properties.

Caudal (1986) developed a formalism in which Jupiter’s magnetic field structure was modelled by solving a magnetostatic equation representing dynamical equilibrium, i.e. a uniformly zero vector sum for all of the aforementioned forces throughout a specified region. This solution was then used to infer the global distribution of current which was consistent with the equatorial distribution of plasma properties such as angular velocity, temperature, density and composition. Caudal (1986) used observations by the *Voyager* spacecraft (Connerney et al. 1981; Bagenal & Sullivan 1981; Krimigis et al. 1981) to constrain this equatorial plasma information, which, in his formalism, acts as a boundary condition for inferring the global plasma properties. The resulting current distribution from such a calculation has a more realistic global structure than the uniformly thick, annular disc used in the empirical models. By including the effects of both plasma thermal pressure and centrifugal force in his formalism, Caudal (1986) naturally extended previous investigations of the distortion of the planetary magnetic field which assumed a cold plasma with negligible thermal energy compared to rotational kinetic energy (e.g. Hill & Carbary (1978)).

The main purpose of this paper is to adapt the formalism by Caudal (1986) in order to model the magnetodisc of Saturn. For the required equatorial plasma properties, we use the latest observations by *Cassini* Plasma Spectrometer (CAPS) (Young et al. 2004) and *Cassini* Magnetospheric Imaging Instrument (MIMI) (Krimigis et al. 2004). The framework, assumptions and inputs for the model are summarised in §2. For the sake of completeness, we provide a derivation of the magnetostatic solution cited by Caudal (1986) in Appendix A. This derivation is not published elsewhere, to the best of our knowledge. Its inclusion here serves as a starting point for discussion of a toy model for the plasmadisc described in §2.2. This model has a very simplified structure in terms of its plasma properties, but serves as a useful illustration of the competition between plasma pressure and centrifugal forces in determining magnetodisc structure. Detailed magnetodisc models for Saturn are presented in §3 and compared with *Cassini* magnetometer (MAG) data from equatorial and high-latitude orbits. A description of MAG is given in Dougherty et al. (2004). These model outputs

are also compared with those of the best-fitting CAN discs. We conclude with a summary and discussion in §4.

## 2 MODEL FRAMEWORK

### 2.1 Magnetic Field Geometry and Force Balance

We adopt the formalism of Caudal (1986), and express the magnetic field components associated with an axially symmetric plasma distribution as gradients of a magnetic Euler potential  $\alpha$ . With this assumption, the magnetic field radial component  $B_r$  and meridional component  $B_\theta$  are

$$\begin{aligned} B_r &= \frac{1}{r^2 \sin \theta} \frac{\partial \alpha}{\partial \theta}, \\ B_\theta &= -\frac{1}{r \sin \theta} \frac{\partial \alpha}{\partial r}, \end{aligned} \quad (1)$$

where  $\theta$  denotes colatitude with respect to the planetary rotation axis (assumed coincident with the magnetic axis), and  $r$  is radial distance from planet centre (in units of planetary radii). The unit of  $\alpha$  in our 'normalised' system is  $B_0 a$ , the product of the equatorial magnetic field  $B_0$  at the planet surface and the planet radius  $a$ . The scales for other relevant physical quantities are shown in Table 1 and Table B1 for the cases of Saturn and Jupiter. Unless otherwise stated, we shall use this dimensionless form of Caudal's original equations in order to easily compare the degree to which different plasma discs may distort the internal field of their parent planets (see also Vasyliūnas (2008) and §3.1).

Caudal (1986) examined the condition of general force balance in the rotating plasma

$$\mathbf{J} \times \mathbf{B} = \nabla P - \frac{1}{2} n m_i \omega^2 \rho \mathbf{e}_\rho, \quad (2)$$

where  $\mathbf{J}$  is current density,  $\mathbf{B}$  is magnetic field and  $\rho = r \sin \theta$  is cylindrical radial distance from the axis ( $\mathbf{e}_\rho$  is the corresponding unit vector). Plasma properties are pressure  $P$ , temperature  $T$  (assumed isotropic and constant along field lines), ion number density  $n$ , mean ion mass  $m_i$  and angular velocity  $\omega$ . In an appropriate corotating frame, this equation represents balance between magnetic force on the left side, and pressure gradient plus centrifugal force on the right. We have not included the minor contribution to plasma mass from the electrons, but do include their contribution to plasma pressure.

Caudal (1986) showed that both the field and current can be derived from  $\alpha$ . When this is done, the force balance condition gives the following partial differential equation:

$$\frac{\partial^2 \alpha}{\partial r^2} + \frac{1 - \mu^2}{r^2} \frac{\partial^2 \alpha}{\partial \mu^2} = -g(r, \mu, \alpha), \quad (3)$$

where  $\mu$  is the cosine of colatitude i.e.  $\mu = \cos \theta$ .

The 'source function'  $g$  is determined by the global distribution of plasma pressure and angular velocity. However, force balance in the direction parallel to the magnetic field implies that the *global* values of these quantities are derivable from their equatorial values and the shape of the magnetic field lines; this is why there is a dependence of  $g$  upon  $\alpha$ . Caudal (1986) derived an analytical expression which could be used to calculate the solution for  $\alpha$ . We have included a full derivation of this expression in the Appendix A. The form involves the use of Jacobi polynomials, which occur as solutions of the homogeneous version of Eq. (3). An important solution in this class is the dipole potential  $\alpha_{\text{dip}} = (1 - \mu^2)/r$ . In practice, we start with a pure dipole potential and then 'perturb'

it using Caudal's iterative method: at every iteration, the 'current' solution  $\alpha_n$  is used to evaluate  $g$  and thus the 'next' solution  $\alpha_{n+1}$ . We stopped our calculations when the difference between successive iterations was at most 0.5 percent. We describe the various inputs used for our Saturn model calculations in §2.3. These are based on a variety of observational studies employing data taken by the *Cassini* spacecraft. Before investigating these Caudalian disc models for Saturn, we shall examine a simple toy model which may be used to predict the effect of a rotating plasma disc upon the zeroth-order (largest-scale) perturbation to the dipole potential.

### 2.2 Toy Model for a Planetary Magnetodisc

We begin our investigation by examining a very simplified model of disc structure. In this model, we assume that the disc has a uniform plasma  $\beta$  parameter denoted  $\beta_h$ , associated with the thermal energy of a hot population. We also assume the presence of an isothermal cold population containing most of the plasma mass, but a negligibly small fraction of the total pressure, with uniform plasma  $\beta$  denoted  $\beta_c$ . Proceeding under these assumptions, it is straightforward to show that Caudal (1986)'s expression for the plasma source function may be written as

$$g(r, \mu, \alpha) = \rho^2 \frac{dP_{h0}}{d\alpha} + \rho^2 \exp\left(\frac{\rho^2 - \rho_0^2}{2\ell^2}\right) \frac{P_{c0}}{\ell^2 B_{\theta 0}}, \quad (4)$$

where  $P_h$  and  $P_c$  denote hot and cold plasma pressure, and the subscript 0 is used to refer to the quantity evaluated at the equatorial crossing point of the magnetic field line, i.e. the magnetically conjugate point for which  $\mu = 0$ . Following Caudal (1986), we assume that the hot component exhibits uniform pressure  $P_h$  all the way along a given field line, while the cold component's pressure is concentrated towards the equatorial plane, according to the exponential factor in Eq. (4). The symbol  $\ell$  thus represents a scale length associated with the cylindrical radial distance  $\rho$ , and is defined by (Caudal 1986)

$$\ell^2 = \frac{2k_b T}{m_i \omega^2 a^2} \quad (5)$$

for a quasi-neutral plasma containing singly charged ions and electrons.  $a$  represents planetary radius and is used here to transform to our normalised system (see Table 1).

Using this definition of plasma scale length, it can be shown that the exponential factor appearing in Eq. (4) has an argument which contains the ratio of an ion's kinetic energy of rotation to its thermal energy. Thus our hot plasma component is defined by ion thermal energies which are large compared to the kinetic energy of rotation at angular velocity  $\omega$  and a consequent scale length which is effectively infinite (large compared to magnetospheric flux tube length). On the other hand, the cold plasma component contains ions with much smaller thermal energies, which cannot compete as effectively with the centrifugal potential in maintaining plasma at locations high above the equatorial plane. We shall see in the later sections that the typical scale lengths for the cold plasma at Saturn are a few planetary radii, a distance which is small compared to the flux tube lengths in the planet's outer magnetosphere.

If we now make the assumption for global magnetic field  $B_{\theta 0} = \rho_0^{-\chi}$  (where e.g.  $\chi = 3$  for a dipolar geometry), then by definition the dependence of normalised magnetic pressure along the equator is given by  $\frac{1}{2} \rho_0^{-2\chi}$ . It follows that  $P_{h0} = \frac{1}{2} \beta_h \rho_0^{-2\chi}$  and  $P_{c0} = \frac{1}{2} \beta_c \rho_0^{-2\chi}$ . Replacing the operator  $\frac{d}{d\alpha}$  with the equivalent  $\frac{-1}{B_{\theta 0} \rho_0} \frac{d}{d\rho_0}$  and assuming uniform  $T$  and  $\omega$ , we may transform

**Table 1.** Physical units used in the normalised (dimensionless) system for both planets.

Planet	Radius ( $a$ )	Magnetic Field ( $B_0$ )	Magnetic Flux ( $B_0 a^2$ )	Pressure ( $B_0^2/\mu_0$ )	Angular Velocity ( $\omega_0$ )
Saturn	60280 km	21160 nT	77 GWb	0.00036 Pa	$2\pi/10.78$ rad h <sup>-1</sup>
Jupiter	71492 km	428000 nT	2187 GWb	0.146 Pa	$2\pi/9.925$ rad h <sup>-1</sup>

the expression for plasma source function from Eq. (4) into the following form:

$$g(r, \mu, \alpha) = \rho^2 \rho_0^{-(\chi+2)} \left[ \beta_h \chi + \frac{\beta_c \rho^2}{2\ell^2} \exp\left(\frac{\rho^2 - \rho_0^2}{2\ell^2}\right) \right]. \quad (6)$$

It is straightforward to show, using Eq. (5), that the term  $(\beta_c \rho^2/2\ell^2)$  is equivalent to the ratio of rotational kinetic energy density to magnetic pressure. It may therefore be thought of as a plasma ‘beta’ for bulk rotation, rather than random ion motions. If we consider the equatorial location of any given flux tube ( $\rho = \rho_0$ ), then we find that the hot and cold plasma contributions to the source function are equal at an equatorial radial distance  $\rho_T$  given by:

$$\rho_T^2 = 2\chi\ell^2(\beta_h/\beta_c). \quad (7)$$

Beyond the transition distance  $\rho_T$  the rotational kinetic energy of the plasma exceeds its thermal energy. Therefore, centrifugal force (in a corotating frame) dominates pressure gradients for distances  $\rho \gg \rho_T$  in determining both the magnetospheric current; and the distortion to the planetary dipole field required to maintain the magnetodisc’s dynamic equilibrium. Conversely, for  $\rho \ll \rho_T$ , the role of rotation is less important and plasma pressure determines disc structure. Interestingly,  $\rho_T$  may conceivably exceed the standoff distance of the dayside magnetopause under conditions where: (i) Hot plasma  $\beta$  is very high compared to the cold plasma; (ii) Plasma angular velocity is adequately low; or (iii) For a given temperature of cold plasma, its density is small (such that the quantity  $\ell^2/\beta_c$  becomes very large). We shall see in the following sections that average magnetospheric conditions at Saturn may yield transition distances at or inside the magnetopause (outer magnetosphere), while for Jupiter the magnetospheric current arises predominantly from hot pressure gradients.

We shall now investigate the relatively simple expression for the magnetic potential of the homogeneous disc model. We make use of the following equality, valid for dipolar magnetic field lines:

$$\rho_0 = r/(1 - \mu^2). \quad (8)$$

Eq. (8) indicates that dipolar field lines have parabolic shapes in the  $(r, \mu)$  co-ordinate plane. By definition,  $\rho^2 = r^2(1 - \mu^2)$  and thus the argument of the exponential factor in (4) may be expressed in terms of  $r$  and  $\mu$ . The full representation of the plasma source function in these co-ordinates can be derived as (eliminating  $\rho_0$  using Eq. (8)):

$$g_D(r, \mu) = r^{-\chi}(1 - \mu^2)^{\chi+1} \left[ \beta_h \chi (1 - \mu^2)^2 + \frac{\beta_c r^2}{2\ell^2} \exp\left(-\frac{r^2}{2\ell^2} \frac{1 - (1 - \mu^2)^3}{(1 - \mu^2)^2}\right) \right]. \quad (9)$$

The source function for our simplified disc structure, Eq. (9), has been derived using a dipolar magnetic field. Therefore it is an appropriate form for magnetic fields which may be decomposed into the planetary dipole plus a small perturbation (in the sense that the perturbation is everywhere small compared to the dipole field strength). In order to provide an approximation for this perturbation field due to the plasma disc, we shall calculate only the zeroth-order

terms in the expansion for the magnetodisc potential described by Eq. (A26). By ‘zeroth-order’, we mean the terms involving the orthonormal basis function  $(1 - \mu^2) P_0^{1,1}(\mu) = (\sqrt{3}/2)(1 - \mu^2)$ , which involves the Jacobi polynomial of order zero. This function represents the largest angular scale of the magnetodisc potential ( $\mu^2$  dependence). The planetary dipole field has this angular dependence and is thus included in the zeroth-order solution.

If we use Eq. (A26) to calculate the zeroth-order part of the potential, in conjunction with the explicit form of the source function for our homogeneous disc. Eq. (9), the resulting expression is:

$$\alpha_0(r, \mu) = (1 - \mu^2)/r \left( 1 + \int_1^r u^2 g_0(u) du + r^3 \int_r^\infty u^{-1} g_0(u) du \right), \quad (10)$$

where we have defined  $g_0$ , the zeroth-order coefficient of the source function  $g_D$ , in terms of radial distance:

$$g_0(r) = \frac{1}{4} \int_{-1}^1 g_D(r, \mu) d\mu. \quad (11)$$

The first factor in Eq. (10) is the unperturbed dipole potential, and the integral terms in the second factor (enclosed by square brackets) represent the lowest-order (largest angular scale) perturbations due to the presence of the model plasma disc. It is evident from the integral limits that any location which lies outside the disc plasma will still experience a magnetic field due to all of the remote disc currents flowing within the radial distance of such a point. Fig. 1 shows contours of equal magnetic potential (i.e. magnetic field lines) for the function  $\alpha_0$  evaluated for three examples of the homogeneous disc model. The first model is a hot disc with  $\beta_h = 1$  and no cold population ( $\beta_c = 0$ ); the second is a cold disc with  $\beta_h = 0$  and  $\beta_c = 0.2$ ; and the third is a combined disc with  $\beta_h = 0.5$  and  $\beta_c = 0.1$ . All the homogeneous discs are assumed to be in perfect corotation with the planet, have uniform length scale  $\ell = 1$  and uniform field strength index  $\chi = 3$ . The disc models have had their structures truncated by setting their source function to zero for regions which are magnetically conjugate to equatorial distances  $\rho_0 < 5$  and  $\rho_0 > 35$ . The field lines of a vacuum dipole are also shown for comparison in the top panel.

The closely-spaced dark grey and light grey field lines indicate regions in each panel which cover the same intervals in magnetic potential. This may also be considered as an interval in magnetic flux, since the total magnetic flux  $\Phi_B$  threading the region from cylindrical radial distance  $\rho$  to infinity is a simple multiple of magnetic potential evaluated at this distance:  $\Phi_B(\rho) = 2\pi\alpha(\rho, Z)$  (where the vertical co-ordinate  $Z = r \cos \theta = r\mu$ ). This relation follows from the definition of the magnetic field components in Eq. (1) (Caudal 1986). We see that the presence of the disc tends to ‘inflate’ the dipolar magnetic field lines and shift them to larger equatorial crossing distances. For the flux tubes highlighted, we see that this effect is quite pronounced for the dipolar field lines which cross 10–12 planet radii ( $R_P$ ) at the equator (shaded light grey). These flux tubes are displaced to equatorial distances 16–25  $R_P$  by the disc models.

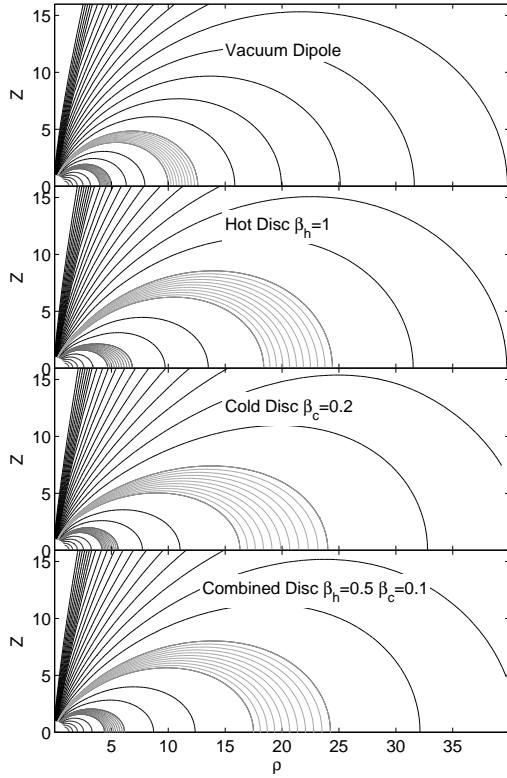


**Figure 1.** Geometry of magnetic field lines for the zeroth-order homogeneous disc models (see text). The solid black lines indicate contours which are spaced by uniform intervals in the logarithm of the magnetic potential. The dark grey and light grey lines indicate regions which lie between the same values of magnetic potential in each panel.

By contrast, the flux tubes shaded dark grey, situated near  $\sim 5 R_P$ , do not undergo as great a distortion in the presence of the disc. This part of the field may be considered as a ‘rigid’, inner magnetosphere dominated by the internal planetary field. We also note that the cold disc model produces outer magnetospheric field lines which are noticeably more oblate in shape compared to the other discs: a field line crossing at a given equatorial distance does not rise as far above the equator in the cold disc model. This property reflects the tendency of the cold plasma disc to be concentrated near the equatorial plane (according to the scale length  $\ell$ ), thus producing stronger distortion in the near-equatorial segments of the model field.

The outer magnetospheric flux tubes in the present example (field lines shaded light grey in Fig. 1) also become spread out over a larger radial distance compared to the dipole configuration. In the upper panel of Fig. 2, we compare the corresponding equatorial profile of field strength between the disc models and the dipole field. For all disc models, the ratio of total to dipole field strength increases monotonically with distance, indicating that the magnetodisc field is more uniform than the dipole. We also see that each model has a characteristic distance which separates an inner region where the field strength ratio  $B/B_{\text{dip}} < 1$  from an outer region where this ratio exceeds unity. This feature is observed in actual planetary ring currents, and arises from the finite extent of the current region and the solenoid-like nature of the corresponding magnetic field (e.g. Sozou & Windle (1970) and Figures 1, 4 and 5 of Arridge et al. (2008b)).

Near the inner boundary of the equatorial disc current, the

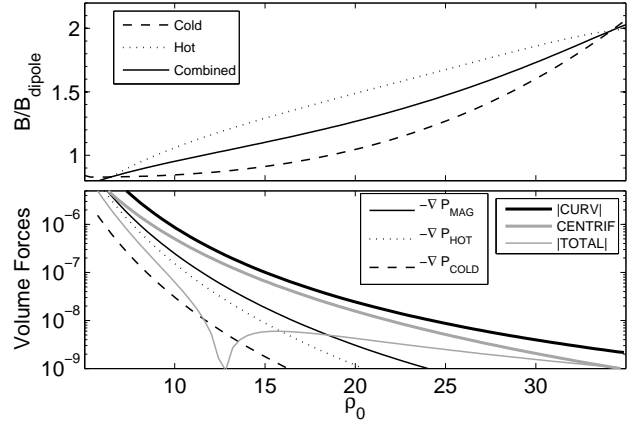


**Figure 2.** Upper panel: field strength in the equatorial plane, relative to that of a pure dipole field, as a function of radial distance  $\rho$ , for various homogeneous disc models (see legend and text). Lower panel: forces per unit volume (dimensionless) in the equatorial plane of the homogeneous, combined disc model, labelled according to line style.

vertical magnetic field generated by this current alone opposes the planetary field, while the opposite is true near the outer disc boundary, where the disc field enhances that of the planetary dipole. We thus expect and find that the ratio of total magnetic field to that of a pure dipole monotonically increases from values less than unity near the inner edge of the disc ( $\sim 5 R_P$ ) to values larger than unity near the outer edge ( $\sim 35 R_P$ ).

We now consider the radial profiles of the main forces involved in the dynamic equilibrium of the homogeneous disc structure. We do not expect these forces to be in perfect balance for our zeroth-order model, since this is only one component of the many required to retrieve the full solution, and corresponds to the largest angular scales of the problem ( $\sin^2 \theta$  dependence). We plot the equatorial centrifugal force, magnetic forces and plasma pressure gradients as a function of distance in the lower panel of Fig. 2 for the homogeneous, combined disc model described above. The plots show us that, for the outer region where the ratio  $B/B_{\text{dip}} > 1$  and  $\rho > 12 R_P$ , the force of highest magnitude is that due to magnetic curvature, followed by centrifugal force (factor of  $\lesssim 2$  smaller than curvature force) and magnetic pressure gradient (factor of  $\gtrsim 5$  smaller than curvature force). The hot plasma pressure has a gradient about half the magnitude or less of that for magnetic pressure, while the weakest force in this model is the gradient due to cold plasma pressure. We see that the sum total of the forces is less than one per cent of the curvature force at  $\rho = 12 R_P$ , and less than ten per cent for  $\rho = 10\text{--}16 R_P$ . This aspect of the total force profile is an indication of the degree to which dynamic equilibrium is maintained within the zeroth-order component of the full solution.

The transition distance for the combined disc model is  $\rho_T \sim 5.5 R_P$ , using Eq. (7). It is also evident from Fig. 2 that, for distances much greater than this value, we are by definition in the part of the magnetosphere where centrifugal force dominates hot plasma pressure, and where the force balance principally involves the centrifugal and magnetic curvature forces. As we approach the transition distance from the outer disc, the other forces due to plasma pressure and magnetic pressure become comparable to curvature force; and thus become more significant in determining stress balance and disc structure.

### 2.3 Model Inputs and Boundary Conditions

In this section, we summarise the model inputs we have used to determine the equatorial boundary conditions for our calculations of the Kronian magnetodisc field. These inputs have been drawn from a variety of observational studies using the plasma instruments aboard the *Cassini* spacecraft. They fall into the following four categories, each described in more detail in the subsections below: (i) Composition; (ii) Temperature and density; (iii) Hot plasma pressure; and (iv) Rotation.

#### 2.3.1 Equatorial Plasma Composition

The equatorial composition of the cold plasma at Saturn is required in the model for the computation of the scale length  $\ell$  (Eq. (5)), assumed constant along magnetic field lines. The composition of the plasma is determined by the relative densities of water group ions (mass  $m_W = 18$  amu) and protons (mass  $m_P = 1$  amu). Following Caudal (1986) we represent the disc ions as having a mean mass  $m_i$  between these two limits, given by:

$$m_i = \frac{n_W m_W + n_P m_P}{n_W + n_P}, \quad (12)$$

where the symbol  $n$  denotes number density, with obvious subscripts indicating water group and proton components. In order to capture the behaviour of  $m_i$  as a function of radial distance, we employed the formulae of Wilson et al. (2008), who determined and fitted density moments for water group ions and protons using observations by CAPS.

Wilson et al. (2008)'s observations sampled five equatorial spacecraft orbits in the distance range  $\sim 5.5$ – $11 R_S$  between October 2005 and April 2006. The orbits were chosen as mission segments during which CAPS ion mass spectrometer obtained sufficient coverage of the plasma particle distribution to allow reliable computation of moments. For the purposes of our modelling, we used the Gaussian fits to water ion density and proton density by Wilson et al. (2008) to compute the following number fraction of protons as a function of radial distance:

$$\frac{n_H}{n_W + n_H} = \frac{f_M(\rho)}{1 + (A_W/A_H) \exp[(B_H - B_W)\rho^2]} \quad (13)$$

$$f_M(\rho) = 0.1 \left[ 1 - \tanh\left(\frac{\rho - 15}{2}\right) \right] + 0.8,$$

where the function parameters provided by Wilson et al. (2008) are  $A_W = 161.5 \text{ cm}^{-3}$ ,  $A_H = 8.3 \text{ cm}^{-3}$ ,  $B_W = 0.042 R_S^{-2}$  and  $B_H = 0.031 R_S^{-2}$ . Since these fitted functions are based on observations in the distance range 5–12  $R_S$ , we used the hyperbolic tangent function  $f_M$  to place the additional constraint that the proton number fraction approaches 80 per cent in the outer magnetosphere. This plasma composition was determined by Arridge et al. (2007) to provide good agreement with both electron densities observed by *Cassini* in the outer magnetosphere and the surface mass density of the Kronian plasma disc. The latter quantity was deduced in the same study from the analysis of magnetic signatures of transient excursions by the spacecraft into the magnetodisc current sheet. Fig. 3 shows plots of the fitted composition profile from Wilson et al. (2008); the extrapolation of this profile beyond the range of validity (5–12  $R_S$ ); the profile used in the current work; and the multiplier function  $f_M$ .

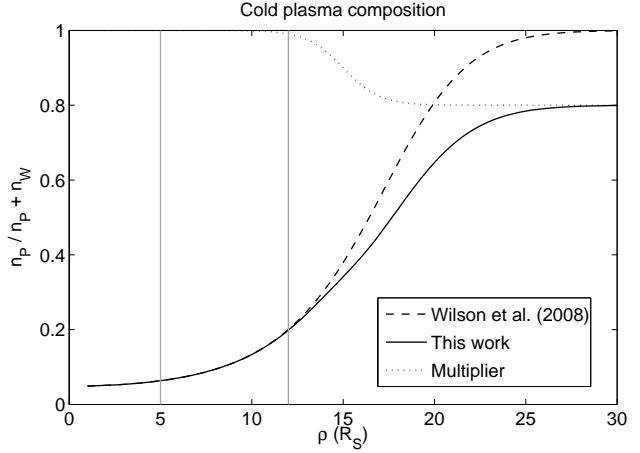


**Figure 3.** Profiles of proton number fraction in the cold disc plasma. Dashed line: profile determined from the fits to plasma density moments by Wilson et al. (2008). Solid line: profile used in this work. Dotted line: the multiplying function used to constrain the outer magnetospheric composition (see text). Vertical lines indicate the range of validity of the fitted functions of Wilson et al. (2008).

#### 2.3.2 Equatorial Plasma Temperature and Density

For the cold plasma population, the contribution to the source function  $g$  (Eq. (3)) takes the form (see also Eq. (4)):

$$g_c(r, \mu, \alpha) = \rho^2 \exp\left(\frac{\rho^2 - \rho_0^2}{2\ell^2}\right) \left(\frac{dP_{c0}}{d\alpha} + \frac{P_{c0}}{\ell^2 B_{\theta 0}}\right), \quad (14)$$

where the geometry of the magnetic field, represented by  $\alpha$ , determines the mapping between  $\rho$  and  $\rho_0$  along a field line, as well as the equatorial field strength  $B_{\theta 0}$ . In order to compute the scale length  $\ell$  in the equatorial plane, we require the equatorial distribution of plasma temperature. Strictly speaking the latter should be the field-parallel temperature, since  $\ell$  is associated with force balance parallel to the magnetic field. In addition, a knowledge of both plasma temperature and density is required to specify the equatorial pressure  $P_{c0}$ .

To satisfy these requirements, we appealed to the study by Wilson et al. (2008) which provided tabulated measurements of both parallel and perpendicular temperature for the thermal water group ions and protons at Saturn. These tabulations contain average temperatures over intervals of radial width  $0.5 R_S$  near the planet's equatorial plane, extending between radial distances 5.5–10  $R_S$ . To obtain total plasma temperatures for modelling purposes, we began by combining the tabulated ion and proton temperature values from Wilson et al. (2008) as follows:

$$T_{\parallel} = \frac{n_W T_{W\parallel} + n_H T_{H\parallel}}{n_W + n_H},$$

$$T_{\perp} = \frac{n_W T_{W\perp} + n_H T_{H\perp}}{n_W + n_H},$$

$$T_c = \frac{T_{\parallel} + 2T_{\perp}}{3}, \quad (15)$$

where  $n_W$  and  $n_H$  are the respective water-group ion and proton number densities from Wilson et al. (2008) (see §2.3.1); the symbol  $T$  represents temperatures; and the subscripts  $\parallel$  and  $\perp$  are associated with thermal motions parallel and perpendicular to the magnetic field. The quantities  $T_{\parallel}$  and  $T_{\perp}$  are average parallel and perpendicular temperatures for the cold plasma (weighted by number density between protons and water-group ions), while  $T_c$  is an ap-

proportionately weighted mean. In Fig. 4 we show plots of the radial profiles of  $k_b T_{\parallel}$  and  $k_b T_c$ , expressed in units of eV. While the data provided by Wilson et al. (2008) are valuable for our work, we still need to assign temperatures to those regions of the magnetosphere outside the reach of this study, i.e.  $\rho_0 < 5 R_S$  and  $\rho_0 > 10 R_S$ . In order to do this, we have assumed that the ion and proton temperatures in these regions are equal to those measured by Wilson et al. (2008) at the closest relevant points (i.e. at  $5.5 R_S$  and  $10 R_S$  respectively). We show these extrapolations as dashed lines in Fig. 4. To obtain the final, realistic input temperature profiles for the cold plasma, we applied second-order polynomial fits to the data-derived profiles of  $T_{\parallel}$  and  $T_c$ . We believe that such an approach is justified in light of the fact that the observations by Wilson et al. (2008) show variability in temperature moments within their  $0.5 R_S$  bins, typically by factors between two and five, even for data from the same orbit. The final fitted profiles are shown as grey curves in Fig. 4.

We used the profiles of  $T_{\parallel}$  in conjunction with our mean ion mass  $m_i$  (§2.3.1) to compute the plasma scale length. We used the  $T_c$  profiles in order to compute the cold plasma pressure in the equatorial plane, according to the following formula, adapted to dimensionless form from Caudal (1986):

$$P_0(\alpha) = 2N_L(\alpha)(k_b T_c)^*/V_W(\alpha). \quad (16)$$

Here, the dependence upon the local value of  $\alpha$  (i.e. the particular field line) is indicated for the dimensionless quantities  $V_W$  and  $N_L$ ; these are, respectively, the weighted unit flux tube volume and the flux tube content. Considering these two quantities for the moment, their definition is based on the usual concept of the unit flux tube volume, which we define in our normalised system as:

$$V(\alpha) = \int_0^{s_B} ds/B, \quad (17)$$

where the integral is taken along a magnetic field line of length  $s_B$  between its southern and northern ionospheric footpoints;  $ds$  is an element of arc length along the field line; and  $B$  is local field strength. Given the relation between equatorial field strength and the increment in magnetic potential (see derivation of Eq. (6)), it follows that  $2\pi V(\alpha) |d\alpha|$  represents the normalised volume between two magnetic shells corresponding to the interval  $[\alpha, \alpha + d\alpha]$ . This same volume is threaded by an increment  $2\pi |d\alpha|$  of normalised magnetic flux.

Using this definition of the unit flux tube volume, we can construct the weighted flux tube volume as follows:

$$V_W(\alpha) = \int_0^{s_B} \exp\left(\frac{\rho^2 - \rho_0^2}{2\ell^2}\right) ds/B, \quad (18)$$

where the exponential weighting factor is a consequence of field-aligned pressure balance for the cold rotating plasma (see also Eq. (6)). The flux tube content  $N_L$  is defined as the number of cold ions per unit of magnetic flux. That is, the quantity  $2\pi N_L(\alpha) |d\alpha|$  is the number of ions within the volume bounded by the magnetic shells corresponding to the interval  $[\alpha, \alpha + d\alpha]$  in magnetic potential.

The factor  $(k_b T_c)^*$  in Eq. (16) is the dimensionless form of the thermal energy corresponding to the averaged plasma temperature  $T_c$  defined in Eq. (15). We obtain this factor through division by the energy scaling factor in Table B1.

By specifying a profile of flux tube content in the Caudalian model rather than density, it is more straightforward to mimic realistic changes associated with a plasma which is ‘frozen-in’ to the magnetospheric field. Our profile for the flux tube content

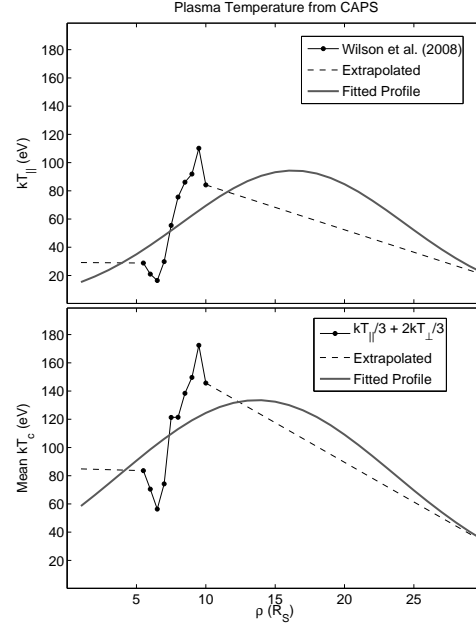


**Figure 4.** Profiles of parallel (top panel) and mean (lower panel) total temperature for the cold disc plasma. Solid lines with dots: total plasma temperatures derived from the moments for water group ions and protons, determined from *Cassini* plasma data by Wilson et al. (2008) (see text). Dashed lines: extrapolated temperature profiles, derived by assuming that the individual ion species have temperatures equal to those at the nearest location in the tabulation of Wilson et al. (2008). Solid grey lines: the final model inputs, obtained by second-order polynomial fits to the temperature profiles derived from the data.

was obtained by fitting estimates of this quantity from the work by McAndrews et al. (2009), extended to cover inner magnetospheric regions 4–10  $R_S$  (H. J. McAndrews, private communication). These authors used *Cassini* nightside near-equatorial plasma observations by CAPS in conjunction with the magnetospheric field model by Khurana et al. (2006) in order to estimate  $N_L$  through a force balance relation similar to Eq. (16). We have fitted the flux tube content measurements with two Gaussian functions, constrained to meet continuously at  $6.5 R_S$ . The entire fitted profile for  $N_L$  used in the model is shown in Fig. 5. In order to bring this profile of flux tube content into reasonable agreement with the density moments provided by Wilson et al. (2008) (who studied orbits distinct from those used by McAndrews et al. (2009)), we multiplied them by a smooth correction function whose shape, but not absolute scale, is also shown in Fig. 5.

### 2.3.3 Hot Plasma Pressure

Caudal (1986) assumed that the hot magnetospheric plasmas filled each flux tube such that each flux tube can be characterised by a particular equatorial pressure  $P_{h0}$  and volume per unit flux  $V$ , referred to as the hot plasma approximation. Using the ideal gas equation per unit flux one can show that the product  $P_{h0}V$  is equal to  $N_0 k_b T_h$  where  $N_0$  is the number of ions per unit flux and  $k_b T_h$  is the mean kinetic energy of the ions (see also §2.3.2). Caudal (1986) used observations from the Jovian magnetosphere to show that  $k_b T_h$  did not vary appreciably with  $L$ . In the absence of plasma sources the time-stationary radial (cross- $L$ ) transport of plasma can be described using a one dimensional diffusion equation. Caudal (1986, and references therein) showed that the plasma tended to

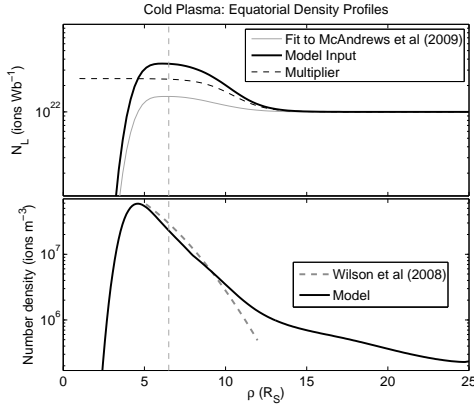


**Figure 5.** Profiles of cold plasma flux tube content (top panel) and number density (lower panel) in Saturn’s equatorial plane. The top panel shows: radial profiles of flux tube content  $N_L$  in ions per Weber for the Gaussian fits to the original observations of McAndrews et al. (2009) (grey line); the shape of the multiplying function used to modify this profile (dashed line, see text); and the final form of the profile used for the disc models (black line). The vertical line shows the division between regions where different Gaussian profiles were used to fit the  $N_L$  data. The lower panel shows the agreement between the ion number density profile from the observational fits of Wilson et al. (2008) with that derived from a disc model with magnetopause radius  $R_{MP} = 25 R_S$ .

have a uniform distribution in  $L$  when the rate of loss of particles due to pitch angle scattering into the loss cone was negligible compared to the rates for cross- $L$  transport. This reasoning led Caudal (1986) to conclude that  $P_{h0}V$  and  $N_0(L)$  were independent of  $L$  and hence that under rapid radial diffusion the hot plasma in the Jovian magnetosphere behaves isothermally rather than adiabatically:  $P_{h0}V^\gamma = \text{const}$  where  $\gamma = 1$ . Caudal (1986) used published energetic particle pressures and magnetic field models in order to show that the particles did indeed behave isothermally beyond  $\sim 18 R_J$ , but adiabatic on smaller  $L$ -shells. In further work, Caudal & Connerney (1989) made  $\gamma$  a free parameter in a fit of the model to Voyager magnetometer data. They found that  $\gamma = 0.88$  beyond  $9 R_J$ , suggesting the presence of non-adiabatic cooling processes during inward diffusion, losses, and violations of the first and second adiabatic invariants.

Following Caudal (1986), we parametrised the distribution of hot plasma pressure in our model by appealing to observations, using the same  $P_{h0}V^\gamma = \text{const}$  theoretical framework. The data required were taken from the study by Sergis et al. (2007), who determined pressure moments for ions with energy  $> 3 \text{ keV}$  from the measurements of MIMI. The observations presented by these authors were acquired within the distance interval  $5 < \rho < 20 R_S$  over eleven consecutive near-equatorial orbits of the spacecraft between late 2005 and early 2006. An important result to emerge was that, within this ‘hot population’, particles with energy  $> 10 \text{ keV}$  carried half of the total pressure, but contributed only  $\sim 10$  percent of the total number density. We shall see in the later sections that the hot plasma pressure for typical conditions at Saturn may exceed that of the colder population (see §2.3.2) by up to an order of magnitude; it was therefore important to include a representation of this hot pressure component in our magnetodisc model’s source function.

We used an empirical magnetic field model to determine the unit flux tube volume  $V(\alpha)$  as a function of  $\rho$ . The empirical model comprised an un-tilted dipole and CAN current sheet, where the

parameters of the model current sheet were dependent on the distance to the subsolar magnetopause (Bunce et al. 2007). We note in passing that the results of this analysis are not significantly altered by using an alternative model, such as Khurana et al. (2006). The second-order fits to plasma  $\beta$  as a function of  $L$  by Sergis et al. (2007) were then used to provide values of the hot plasma pressure  $P_{h0}$  at the equator, using the model magnetic field strength to calculate pressure from plasma  $\beta$ . The results are presented in Fig. 6a, where we show  $P_{h0}$  as a function of  $V(\alpha)$  for the three different fits to the highly-variable hot pressure data presented by Sergis et al. (2007), which they referred to (in order of increasing plasma  $\beta$ ) as the quiescent (blue), average (black) and disturbed (red) ring current. The shaded regions indicate the variability introduced by modifying the subsolar standoff distance of the magnetopause which modifies the parameters of the CAN model (Bunce et al. 2007). By comparison between the calculations and the isotherms (solid) and adiabats (dashed) one can see that there is only a very narrow region in  $L \sim 12\text{--}16 R_S$  where the transport can be considered to be either isothermal or adiabatic. Inside  $9 R_S$  Saturn’s neutral OH cloud is a strong absorber of energetic particles and losses might reasonably account for the decrease in pressure at smaller values of  $L$  (and  $V(\alpha)$ ). In support of this, it is known that the hot oxygen temperature is approximately constant with  $L$  (Dialynas et al. 2009) and that the hot oxygen contributes the most to the hot pressure  $P_{h0}$ . Hence, a reduction in pressure is related to a decrease in the number of hot oxygen ions per unit flux. At larger distances the pressure varies more steeply than  $P_{h0}V(\alpha)^{5/3}$  suggesting a reduction in pressure. This may be related to the observed warping of the magnetic equator (Arridge et al. 2008a) which implies that particle pressures measured in the rotational equator will be smaller than at the magnetic equatorial plane. Energetic particle pressures beyond  $20 R_S$  presented by Sergis et al. (2009) support the fact that the pressure appears to be underestimated by the fits in Sergis et al. (2007).

The product  $P_{h0}V(\alpha)$  was also determined as a function of  $\rho$  and shown in figure Fig. 6b. As expected,  $P_{h0}V(\alpha)$  increases linearly with  $L$  within, and just beyond Saturn’s neutral cloud, due to the increasing flux tube volume and pressure and peaks near  $13\text{--}15 R_S$  before falling with increasing  $L$ . Using the pressures published by Sergis et al. (2009) and the calculated flux tube volumes beyond around  $16 R_S$  the value of  $P_{h0}V(\alpha)$  for  $L > 16 R_S$  is greater than  $\sim 5 \cdot 10^5 \text{ Pa m T}^{-1}$ . Nevertheless, the entirety of the  $P_{h0}V(\alpha)$  profiles reflects the strong variability in hot plasma  $\beta$  for Saturn’s magnetosphere. It is important to note in this context that the different ring current ‘states’ for plasma  $\beta$  fitted by Sergis et al. (2007) represent the range of values of this parameter over several different orbits and magnetospheric configurations, as well as a wide range of radial distances and local times within each orbit.

In view of the strong variability in this parameter and its general decline with decreasing distance inside  $\sim 10 R_S$ , we adopted a simple representation for its global behaviour, similar to that of Caudal (1986). We composed a profile of  $P_{h0}$  by setting the product  $P_{h0}V(\alpha)$  to a constant value  $K_h$  beyond  $\rho = 8 R_S$ ; and by decreasing hot pressure linearly with decreasing  $\rho$  inside this distance, according to the formula  $P_{h0}(\rho) = P_{h0}(8 R_S) \times (\rho/8)$ . We then retrieved  $P_{h0}$  values in our model’s outer magnetosphere beyond  $8 R_S$  through  $P_{h0} = K_h/V(\alpha)$ . This form gives a more realistic response of the value of hot pressure to different configurations of the outer magnetosphere (from expanded to compressed) than would a single function of  $\rho$  alone. In addition, the parameter  $K_h$  gives a compact representation of the ‘level of activity’ of the

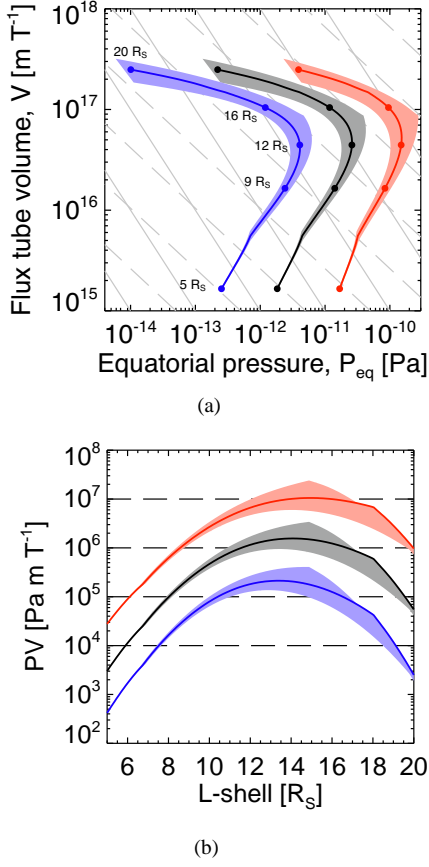


**Figure 6.** Hot plasma pressure  $P_{h,0}$  as a function of unit flux tube volume  $V(\alpha)$  in MKS units (panel a) and the product of hot plasma pressure and unit flux tube volume as a function of  $L$  (panel b) in Saturn's equatorial plane. The coloured curves employ the fitted pressure profiles determined by Sergis et al. (2007) to the highly variable pressure data from MIMI. The colours represent the disturbed (red), average (black) and quiescent (blue) ring current states, in the parlance of these authors. The solid coloured curves represent the profiles for a nominal magnetopause standoff distance of  $25 R_S$  and the shaded regions represent the variability introduced into these profiles due to the changing upstream solar wind dynamic pressure affecting the global magnetic field configuration. In panel (a) the solid lines represent isotherms and the dashed lines are adiabats. Particular  $L$ -shells are indicated by the solid dots and annotation. In panel (b) the horizontal dashed lines are reference curves showing the typical range of this quantity in the outer magnetosphere of Saturn.

ring current in the model. We intend to pursue a future parametric study of disc structure dependent on this parameter and magnetopause radius. For the purpose of this introductory study, we set the value  $K_h = 2 \cdot 10^6 \text{ Pa m T}^{-1}$  in our calculations (the scaling factor for normalised  $K_h$  is given in Table B1). This value according to Fig. 6 represents a ring current somewhat more ‘disturbed’ than the average state.

### 2.3.4 Plasma Rotation

Eq. (4) for the plasma source function includes the scale length  $\ell$ , itself dependent on the angular velocity of the cold rotating plasma at each point along the equatorial plane. Under the steady-state assumption of the model, this angular velocity  $\omega$  is constant along a magnetic field line, i.e.  $\omega$  is expressible as a function of  $\alpha$  alone.

Thus it is observations of plasma  $\omega$  which we seek in order to complete the equatorial boundary conditions for our model calculations.

To construct a model for the azimuthal velocity  $v_\phi$  of the plasma we used data from studies by Kane et al. (2008) and Wilson et al. (2008). The study by Kane et al. (2008) provided measurements of  $v_\phi$  through analysis of ion velocity anisotropies, acquired in Saturn's outer magnetosphere by ion-neutral camera (INCA), a detector of MIMI. As well as the estimated uncertainty of  $\sim 20$  percent in their individual velocity measurements, Kane et al. (2008)'s results also show considerable variability, around factors of two, within subsets of their measurements acquired near the same radial distance. This variability is attributable to the underlying set of spacecraft orbits sampling different local times and magnetospheric configurations (e.g. the INCA data used were obtained in the dawn sector for  $\rho < 25 R_S$  and in the midnight sector outside this distance). Following a different approach with a different data set, Wilson et al. (2008) determined  $v_\phi$  by fitting drifting bi-Maxwellian velocity distributions to CAPS ion mass spectrometer data. They presented quadratic fits of  $v_\phi(L)$  for the region between  $5.5$  and  $\sim 10 R_S$ .

While a fully self-consistent model would include the influence of magnetospheric configuration on the profile of  $v_\phi$  and angular velocity  $\omega$ , we shall address this issue in a future study. For the present purpose, we use a profile of  $v_\phi$  versus  $\rho$  obtained by fitting a sixth-order polynomial to points from the model of Wilson et al. (2008) and points taken from Figure 4 of Kane et al. (2008). Inside of  $3.1414 R_S$  we assumed the plasma is in ideal corotation with an angular velocity of  $1.638 \cdot 10^{-4} \text{ rad s}^{-1}$  (a period of  $10.65 \text{ h}$ ). The  $v_\phi$  and  $\omega$  profile corresponding to this fit are illustrated in Fig. 7. Note that whilst the modelled velocity is slightly smaller than the mean velocities presented by Kane et al. (2008) in the outer magnetosphere, plasma velocities presented by McAndrews et al. (2009) are slightly lower than Kane et al. (2008) and so the model is fully consistent with the published azimuthal velocities acquired by *Cassini*. For further comparison, we include the *Voyager* velocity measurements by Richardson (1998) in the Figure. At distances smaller than  $\sim 10 R_S$ , the model curve agrees well with the *Voyager* data. Beyond this distance, the model has values higher than the mean *Voyager* values, but is still consistent with the full range of these measurements.

For the information of other modellers, we also present here the seven-element vector  $\mathbf{C}$  of polynomial coefficients for the fitted plasma velocity profile. The following coefficients generate  $v_\phi$  in  $\text{km s}^{-1}$ :

$$v_\phi(\rho) = \sum_{n=0}^6 C_n \rho^n, \quad \rho \geq 3.1414 R_S,$$

$$\begin{aligned} C_0 &= -15.09, & C_1 &= 28.16, \\ C_2 &= -6.359, & C_3 &= 0.7826, \\ C_4 &= -0.043, & C_5 &= 1.065 \cdot 10^{-3}, \\ C_6 &= -9.762 \cdot 10^{-6}. \end{aligned} \quad (19)$$

## 3 MAGNETODISC MODELS

Having described our methods for incorporating equatorial observations of plasma properties into the Caudalian model formalism, we now turn our attention to some example model outputs and how such calculations may be used to infer some important physical aspects of magnetodisc structure at Saturn. We shall firstly consider

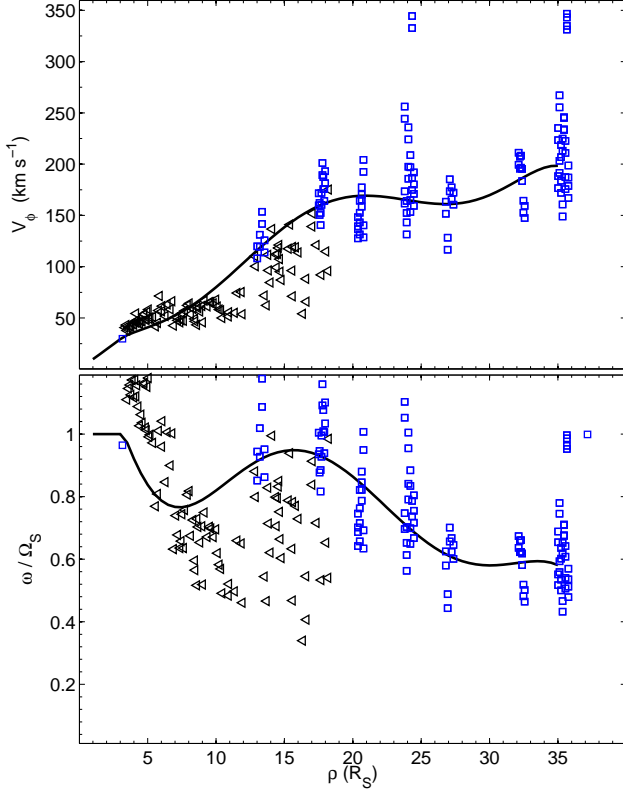


**Figure 7.** Upper panel: A polynomial fit of order six for the azimuthal plasma velocity (thick solid curve) compared with observations of the plasma azimuthal velocity in Saturn’s magnetosphere (squares, Kane et al. (2008); triangles, Richardson (1998)); Lower panel: The same comparison in the upper panel is shown with the azimuthal velocity transformed to angular velocity in the models and observations.

some aspects of force balance in a disc formed under average solar wind pressure conditions and magnetopause size as observed in the *Cassini* era.

### 3.1 Magnetodisc Structure for Average Magnetopause Size

The probability distribution of magnetopause standoff distance at Saturn was determined by Achilleos et al. (2008) who surveyed magnetopause crossings of the *Cassini* spacecraft during 16 orbits between July 2004 and September 2005. The mean standoff distance for this interval was found to be  $\sim 25 R_S$ . We thus adopt this value for our present work as an appropriate magnetopause radius for a nominal magnetodisc model representing average solar wind conditions at Saturn.

The presence of the magnetopause boundary requires a corresponding contribution to the magnetic potential  $\alpha$  from the currents flowing on that boundary. Caudal (1986) represented this magnetopause potential at Jupiter as the Euler function corresponding to a globally uniform, southward-directed field  $B_S$ , referred to as the ‘shielding field’. Caudal (1986) chose the magnitude of  $B_S$  by requiring that the magnetic flux due to the shielding field, integrated over the entire equatorial plane, be equal to a prescribed fraction  $\xi$  of the total magnetic flux exterior to the boundary due to the planetary plus disc sources. The addition of the shielding potential to the solution for  $\alpha$  at each iteration thus ‘compresses’ the flux tubes of

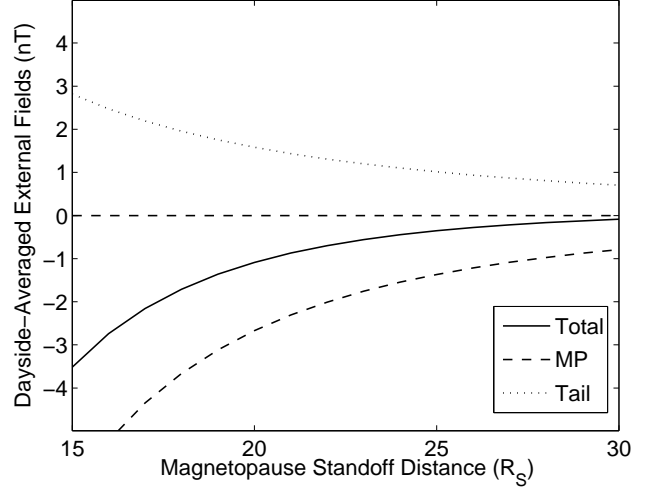


**Figure 8.** Dayside-averaged equatorial values of the shielding magnetic fields associated with Saturn’s magnetotail current sheet (‘Tail’) and magnetopause currents (‘MP’). The field value shown is the  $Z$  component, i.e. positive northward. The global fields used for the averaging were calculated using the formulae of Alexeev et al. (2006) for the configuration where the planetary dipole is orthogonal to the upstream solar wind.

the outer magnetosphere inwards from their ‘boundary-free’ configuration.

For the magnetopause contribution in our axisymmetric models, we adopted a similar approach to Caudal (1986); however, we determined our value of the uniform field  $B_S$  by performing day-side equatorial averages of the empirical field models described by Alexeev & Belenkaya (2005); Alexeev et al. (2006), which represent contributions from both the magnetopause and magnetotail current sheets at Saturn. These two contributions are oppositely-directed (magnetopause field southward, magnetotail field northward). We computed our shielding field as a function of  $R_{MP}$ , using the following parameters to represent approximate conditions at Saturn, as required in the expressions of Alexeev et al. (2006): (i) Planetary dipole orthogonal to the solar wind flow direction; (ii) Radial distance  $R_T$  of the inner edge of the tail sheet equal to  $0.7 R_{MP}$ ; (iii) Magnitude of field in the tail lobe given by  $B_L = \Phi_L R_{MP}^{-2} / [\frac{\pi}{2} (1 + 2R_T/R_{MP})]$ , with open magnetic flux  $\Phi_L = 40 \text{ GWb}$ . The resulting magnetopause contributions, before global averaging, showed variation by a factor  $\sim 2\text{--}3$  between noon local time (strongest field) and the dawn / dusk meridian. The magnetotail contribution showed similar relative variability but with the strongest fields situated at dawn / dusk. Thus in the full representation there are local times where the two contributions add to zero. The uniform (dayside-averaged) shielding field used in our model is shown as a function of  $R_{MP}$  in Fig. 8. We show the contributions to the total shielding field from the magnetopause and tail currents. It is evident that for Saturn the magnetopause currents dominate the shielding field for the more compressed magnetosphere. For the more expanded configuration, the presence of tail currents significantly decreases the shielding field magnitude below its predicted values from magnetopause currents alone.

Several output parameters associated with our average model ( $R_{MP} = 25 R_S$ ) for the Kronian magnetodisc are depicted on a colour scale in the panels of Fig. 9. Fig. 9(a) shows contours of constant magnetic potential  $\alpha$ , equivalent to magnetic field lines, for the vacuum dipole used to represent Saturn’s internal field in

our model. We may compare this geometry with the average magnetodisc model in Fig. 9(b) which corresponds to magnetopause radius  $R_{MP} = 25 R_S$ . The radial stretching of field lines compared to the dipole model becomes particularly pronounced beyond  $\sim 8 R_S$ . For example, the magnetic flux contained between the equatorial distances 6–10  $R_S$  in the dipole field becomes spread out over a larger interval 8–18  $R_S$  in the full magnetodisc solution. We shall compare the equatorial field profiles for these models later in this section.

We now consider Fig. 9(c), which shows the distribution of total plasma pressure in the  $(\rho, Z)$  plane. The scale length  $\ell$  for the model ranges between 1–5  $R_S$  through the magnetosphere, monotonically increasing with  $\rho$ . The pressure contours which attain separations from the equatorial plane significantly larger than these scales are primarily due to the hot plasma pressure, which we have assumed to be uniformly distributed along field lines. One can also see the influence of the equatorial confinement of the cold population, by comparing individual contours with the field line shapes: the pressure contours tend to be more oblate.

Fig. 9(d) shows the magnetic pressure distribution, along with contours of plasma  $\beta$ , which clearly show the influence of the equatorial confinement of the cold population for  $\beta$  of the order unity or larger. The contours of magnetic pressure turn inwards towards the planet as they approach the equator. This is a consequence of force balance perpendicular to the radially-stretched field lines just outside the equatorial plasma disc (e.g. Kivelson & Southwood (2005)). The main forces acting in this direction (which is approximately perpendicular to the equator) are the plasma and magnetic pressure gradients. To maintain balance as the disc is approached, the corresponding increase in plasma pressure must be balanced by decrease in magnetic pressure; hence the behaviour of the magnetic pressure contours. We thus expect total plasma plus magnetic pressure to be constant along the vertical direction near the disc. Fig. 9(e) shows contours of this total pressure, and confirms that they follow directions nearly perpendicular to the equator.

We shall continue our present investigation of average plasmasphere structure at Saturn by considering the model's equatorial properties of magnetic field and force balance in Fig. 10. The upper and middle panels compare the equatorial profiles of magnetic field strength associated with the planetary internal dipole, and with our full magnetodisc solution for average magnetopause size. As for the simple zeroth-order disc models (§2.2), the presence of the plasmasphere produces a total field profile somewhat weaker than the parent dipole for the regions closest to the planet; and stronger than dipole field beyond a characteristic transition distance. The bottom panel of Fig. 10 shows the equatorial profile of positive (radially outward) volume forces. We emphasise here that we have used the *negative* of the curvature force in this plot so that it appears as a positive-valued function. Over most of the model magnetosphere the curvature force is the principal, inward-directed (i.e. negative radial) force. The sum of all the radial forces in the equatorial plane has a magnitude less than 0.2 percent of the local curvature force; this fraction thus provides some measure of the degree of accuracy with which the model can simulate perfect force balance.

The bottom panel of Fig. 10 also indicates which forces dominate the balance and determine disc structure in different regions of the equatorial magnetosphere. Throughout the magnetosphere, the magnetic curvature force is the strongest inward-directed force. For distances  $\rho \gtrsim 15 R_S$ , centrifugal force is higher than plasma pressure gradients by factors up to five, and is therefore the second most important term in the disc's stress balance. Closer to the planet, for  $\rho \sim 6$ –12  $R_S$ , centrifugal force and plasma pressure gra-

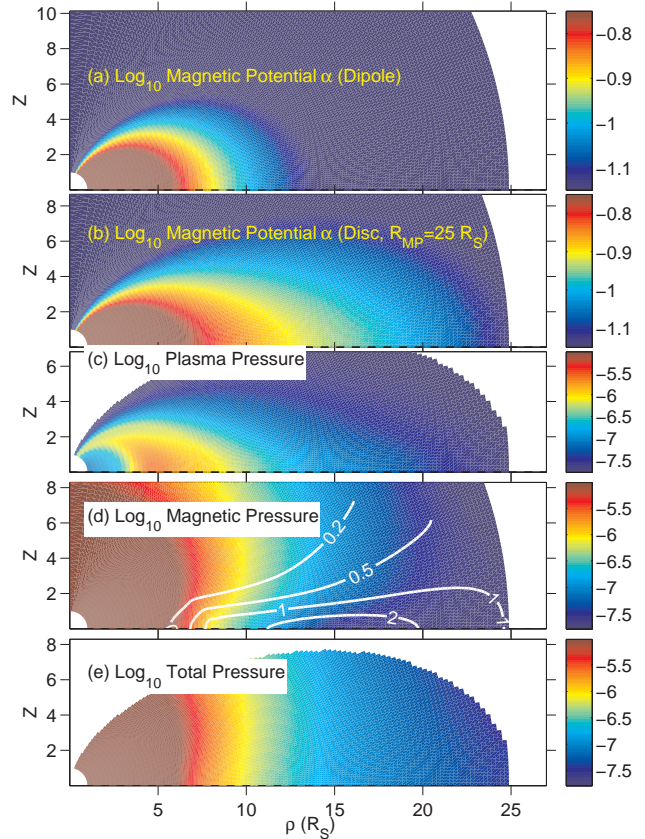


**Figure 9.** (a) Logarithm of magnetic potential  $\alpha$  for vacuum dipole configuration, shown on a colour scale as a function of cylindrical co-ordinates  $\rho$  and  $Z$ ; (b) Logarithm of magnetic potential for an average magnetodisc field model for Saturn, with magnetopause radius 25  $R_S$  and hot plasma index  $K_h = 2 \cdot 10^6 \text{ Pa m T}^{-1}$  (see text); (c) Distribution of plasma pressure within the model from (b); (d) Distribution of magnetic pressure within the model from (b), along with labelled contours of constant plasma  $\beta$  (thick white lines); (e) Total (plasma plus magnetic) pressure on a colour scale. The approximately vertical pressure levels near the equatorial plasma disc are a consequence of force balance perpendicular to the magnetic field (see text).

dients are comparable in magnitude, and the disc's field structure is determined by both sources of radial stress in approximately equal measure. These calculations are in broad agreement with the conclusions of Arridge et al. (2007) who used current sheet crossings to show that centrifugal and pressure gradient forces were approximately equal in magnitude at 20  $R_S$  whereas the model shows the centrifugal forces slightly larger at about twice that of the pressure gradient forces.

Our average Kronian disc model contains a hot plasma pressure distribution which is indicative of a 'mildly disturbed' ring current (see Fig. 6). We therefore would expect hot plasma pressure to play a more dominant role in magnetospheric force balance under conditions of so-called 'disturbed' ring current, as shown by the *Cassini* observations (Sergis et al. 2007). We defer a detailed investigation of this aspect to a future study, and concentrate here on modelling conditions characteristic of the mean level of observed hot pressure.

Fig. 10 shows a small 'kink' in the magnetic force profiles around 8  $R_S$ ; this is due to the sharp linear decrease we have assumed for characterising the product of hot plasma pressure and

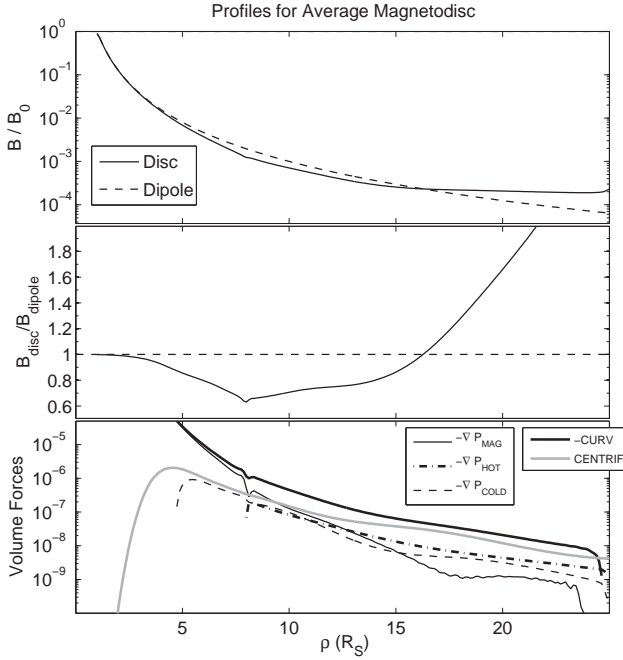


**Figure 10.** Upper panel: Equatorial profiles of magnetic field strength for the planetary dipole alone and for the full magnetodisc solution ( $R_{MP} = 25 R_S$ ); Middle panel: The ratio of the magnetodisc to the dipole field, computed using the profiles in the upper panel; Bottom panel: Normalised volume forces in the equatorial plane of the model, labelled according to line style. We only plot the regions where the force profiles are positive on the logarithmic scale (the negative of the curvature force is used here to demonstrate the balance between it and the other forces).

unit flux tube volume (§2.3.3). The termination at this distance of the curve representing outward-directed force due to hot plasma pressure confirms a sharp change in the sign of the hot pressure gradient; this feature in turn corresponds to the rapid decline with decreasing distance of the modelled hot plasma density. The kink feature is thus somewhat artificial, but does not affect the validity of the global features of our modelled force profiles.

We now consider the inner magnetospheric region ( $\rho \lesssim 6 R_S$ ) depicted in Fig. 10. Inside this distance, the cold plasma population density rapidly decreases (as also shown by the behaviour of the centrifugal force, which is proportional to cold plasma pressure). This magnetospheric region is then characterised by a relative absence of plasma, which explains why the magnetic curvature force and pressure gradient cancel each other: the ensuing signature of the curl-free, unperturbed dipole field.

We conclude this section on average magnetodisc structure at Saturn by investigating the relationship between the previously-considered forces which act to create the magnetodisc geometry and the magnetospheric currents which flow in response to the presence of those forces. On a microscopic scale, we expect the main azimuthal currents to arise from drift motions associated with: (i) Finite plasma pressure (gradient and curvature drifts); (ii) Centrifugal force associated with plasma rotation (inertial current) (e.g. Bunce et al. (2007)). The macroscopic formalism of the model allows an alternative identification of these currents from force balance considerations, as follows. Caudal (1986) pointed out that the source function  $g$  associated with the disc plasma, Eq. (4), could be used to derive the azimuthal current density  $J_\phi$  according to the

following equality:

$$J_\phi(r, \mu) = g(r, \mu) [(r^2(1 - \mu^2))]^{-1/2}. \quad (20)$$

For our Saturn model, the relevant scaling factor for  $J_\phi$  is listed in Table B1. In order to separate the contribution of a particular force to the current density, we simply substitute its corresponding contribution to the source function Eq. (4) for the function  $g$  used in Eq. (20).

Following this method, we calculated the various contributions to azimuthal current in the equatorial plane of the average magnetodisc model. Profiles of positive  $J_\phi$  (in the direction of planetary rotation) are shown on a logarithmic scale in the upper panel of Fig. 11. It is clear that the force which is associated with the dominant contribution to the magnetospheric current depends on radial distance. For example, we note that there is a broad local maximum in the centrifugal inertial current centred at  $\sim 16 R_S$ . This feature corresponds to a similar local maximum in plasma angular velocity according to the model profile from Fig. 7. The lower panel of Fig. 11 shows equatorial profiles of plasma  $\beta$  along with an equivalent  $\beta$  for the rotating disc plasma, computed as the ratio of the rotational kinetic energy density to the magnetic pressure. This rotational plasma  $\beta$  also peaks near  $\sim 16 R_S$ , thus indicating that the dominant term to the plasma source function (and therefore azimuthal current) in this region is the centrifugal force term. Rotational  $\beta$  then decreases for  $\rho > 16$  due to the decline in cold plasma density. The corresponding effect on the current density profiles is a smaller ratio in the outer magnetosphere of the centrifugal to plasma current density.

In the region  $\rho \sim 8\text{--}12 R_S$ , we see from Fig. 11 that the current due to total plasma pressure gradient slightly exceeds the centrifugal current. The hot plasma current is an important factor here; the observed strong variability in hot plasma pressure at Saturn (§2.3.3, Sergis et al. (2007); Krimigis et al. (2007)) implies that differing levels of ring current activity may plausibly increase the radial extent of this region where plasma pressure dominates magnetospheric current, or even lead to its *disappearance*. Inside  $8 R_S$  the hot plasma density sharply decreases and the corresponding decrease in the associated current profile produces an inner region where centrifugal current is once more the major contribution. We shall defer a detailed investigation of the influence of hot plasma index  $K_h$  (§2.3.3) on magnetospheric current profiles to a future study. For present purposes, we note that the calculations indicate it is expected to play a significant role in determining the extent of the region where hot plasma pressure is the major source of the azimuthal current density.

Alongside the modelled plasma  $\beta$  in the lower panel of Fig. 11, we also show observed values of hot plasma  $\beta$  by Sergis et al. (2007, 2009) (grey solid and dashed curves). The dashed grey curves indicate fits to hot plasma observations by Sergis et al. (2007), which show the variation in hot plasma  $\beta$  between average and disturbed ring current states (see also §2.3.3). The solid grey curve was determined from a more recent fit to the median equatorial values of hot plasma  $\beta$  at Saturn determined by Sergis et al. (2009) (computed over  $\sim 0.1 R_S$  intervals), who included the significant contribution ( $\sim 50$  percent) to hot pressure due to  $O^+$  ions. If we compare this curve with the median profile from the earlier study (light grey dashed curve), we see that this inclusion has significantly increased the hot plasma  $\beta$  which would characterise an average state of the ring current. Given this result, and the large intrinsic variability in observed hot plasma pressures, we believe that our simplified model distribution of hot plasma  $\beta$  (red curve) is in reasonable agreement with the expected global be-

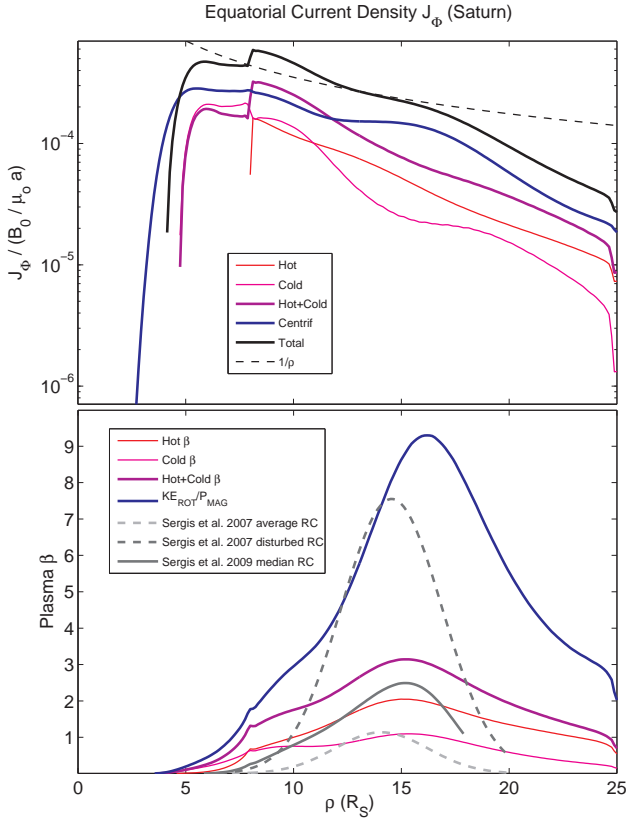


**Figure 11.** Upper panel: Equatorial profiles of positive azimuthal current density taken from the Saturn magnetodisc model with  $R_{MP} = 25 R_S$ . The profiles are plotted on a logarithmic scale and are colour-coded according to the force with which they correspond in the plasmadisc's dynamical balance (hot / cold plasma pressure, centrifugal force). A function proportional to  $1/\rho$  is also shown in order to indicate the form assumed for the current density in the CAN annular disc model Connerney et al. (1981); Lower panel: Equatorial profiles of plasma  $\beta$  taken from the Saturn magnetodisc model with  $R_{MP} = 25 R_S$ . Profiles are colour-coded according to the physical origin of the energy density used to compute the  $\beta$  ratio (hot / cold plasma pressure, rotational kinetic energy). The dashed and solid grey curves show the plasma  $\beta$  profiles fitted to observations of the hot plasma pressure at Saturn obtained by Sergis et al. (2007, 2009).

haviour of this parameter. For the region  $\rho \gtrsim 20 R_S$  our modelled hot plasma  $\beta$  is in excess of the declining values of Sergis et al. (2007, 2009); however, the distant magnetospheric observations by Krimigis et al. (2007) (see Fig. 6) do show hot plasma  $\beta$  which are consistent with our choice for  $K_h$ . Improved future determinations of plasma moments will no doubt enable us to further refine our plasma parametrisation, but for the present study we shall remain with the description given in §2.3.3.

Another important feature of the plasma  $\beta$  profiles in Fig. 11 is the relatively uniform ratio of  $\sim 2$ – $3$  in the outer magnetosphere ( $\rho \gtrsim 15 R_S$ ) between hot and cold plasma  $\beta$ . Our calculations also show that in this region the length scale  $\ell$  for the cold disc plasma (Eq. (5)) monotonically increases with distance between  $\sim 3$ – $5 R_S$ . If we use these values in Eq. (7) for the transition distance in a homogeneous plasma disc between pressure- and centrifugally-dominated regions, we obtain  $\rho_T \sim 12$ – $22 R_S$ . This range of transition distances is consistently smaller than the model magnetopause radius. The actual transition distance for the model appears to be situated at  $\sim 12 R_S$ , beyond which distance

the centrifugal current persistently exceeds total plasma pressure current. The homogeneous disc predictions for  $\rho_T$  thus suggest that the actual value of this distance is expected to lie within Saturn's magnetosphere, and the full magnetodisc model confirms that this is indeed the case. The formula in Eq. (7) therefore provides a reasonable means of estimating the order of magnitude of  $\rho_T$  from observed and / or theoretical properties of the magnetospheric plasma.

We now make a comparative investigation of general magnetodisc structure by comparing the profiles in Fig. 11 for Saturn's plasmadisc with those shown in Fig. 12 for Jupiter. The results in Fig. 12 reproduce the model calculation by Caudal (1986) for a Jovian magnetodisc with magnetopause radius  $R_{MP} = 80 R_J$ . The most striking difference between the Jupiter model and Saturn model is the clear dominance of the Jovian outer magnetosphere's equatorial current density by hot plasma pressure. The hot plasma current is the major contribution to total  $J_\phi$  for distances beyond  $\sim 40 R_J$ . We also note a much stronger contrast between hot and cold plasma  $\beta$  for Jupiter compared to Saturn. While the ratio  $\beta_h/\beta_c$  is an order of magnitude or more beyond  $\sim 40 R_J$  in the Jovian model, the same quantity is  $\lesssim 2$  in the Kronian calculation. As a result, the current profiles due to hot and cold plasma pressure gradients show generally comparable values at Saturn, while at Jupiter the cold plasma current is an order of magnitude or more weaker compared to that of the hot plasma.

These results indicate that the much more expanded magnetosphere of Jupiter develops an outer region beyond  $\sim 40 R_J$ , where the cold plasma's angular velocity and density decline at a rate sufficiently rapid to produce a plasma whose main energy content arises from the thermal motions of the hot particle population. Near  $\sim 27 R_J$  in the Jovian model, the rotational plasma  $\beta$  exceeds the hot plasma  $\beta$  and centrifugal current becomes comparable to hot plasma current. This is qualitatively similar to the corresponding behaviour near  $\sim 16 R_S$  in the Kronian model. If we repeat the exercise of computing the transition distance  $\rho_T$  for the values of plasma  $\beta$  and scale length from the Jovian model, we obtain distances in excess of  $R_{MP}$  well inside the magnetosphere at  $\rho > 40 R_J$  (where  $\ell = 5$ – $40 R_J$ , increasing with distance). This indicates that the centrifugal current at Jupiter should never exceed the hot plasma current in the outer magnetosphere, according to the simple homogeneous disc model. The full magnetodisc model we have presented for Jupiter confirms this prediction, showing a hot plasma-dominated magnetospheric current beyond  $40 R_J$ .

We now consider the relative magnitudes of the magnetospheric current at Jupiter and Saturn predicted by the models. Both Fig. 11 and Fig. 12 show normalised current densities, expressed using scale factors of  $280 \text{ nA m}^{-2}$  (Saturn) and  $4800 \text{ nA m}^{-2}$  (Jupiter) (see Table B1). Although the absolute value of the scale current at Jupiter is much higher because of that planet's stronger internal field, we note something interesting when we compare the normalised current densities at both planets within the same distance range of  $< 25$  planetary radii: the values of normalised  $J_\phi$  at Saturn over  $5$ – $16$  planetary radii exceed those at Jupiter by factors of  $\sim 5$ . Since the distance scale is similar for both models, we conclude that this feature is an indication that Saturn's ring current produces a stronger *relative* perturbation to the planet's internal dipole within this distance range. Interestingly, Vasyliūnas (2008) arrived at a similar conclusion by considering the plasma outflows near the orbital distances of Io and Enceladus ( $\sim 6$  and  $\sim 4$  planetary radii, respectively) and demonstrating that these flows would be expected to produce a stronger relative distortion of the planetary dipole for Saturn.

Our model calculations also show a spatial profile of total  $J_\phi$

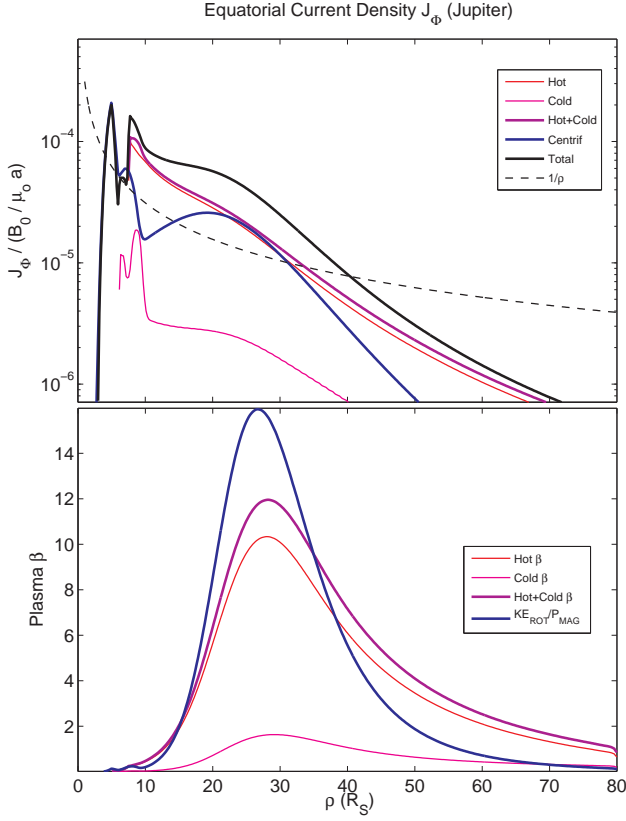


**Figure 12.** Upper panel: Equatorial profiles of positive azimuthal current density taken from the Jupiter magnetodisc model with  $R_{MP} = 80 R_J$  (reproduction of the calculation by Caudal (1986)). The profiles are plotted on a logarithmic scale, and are colour-coded according to the force with which they correspond in the plasmadisc’s dynamical balance (hot / cold plasma pressure, centrifugal force). A function proportional to  $1/\rho$  is also shown in order to indicate the form assumed for the current density in the CAN annular disc model Connerney et al. (1981); Lower panel: Equatorial profiles of plasma  $\beta$  taken from the Jupiter magnetodisc model with  $R_{MP} = 80 R_J$ . Profiles are colour-coded according to the physical origin of the energy density used to compute the  $\beta$  ratio (hot / cold plasma pressure, rotational kinetic energy).

in the outer magnetosphere, for both Jupiter and Saturn, which falls off more steeply with radial distance  $\rho$  than the  $1/\rho$  dependence used by the CAN current disc model. This is an important point of comparison, as it indicates that an outer plasmadisc structure obeying radial stress balance has a characteristic spatial gradient in current density which is significantly different to that usually assumed in ring current modelling studies. Despite this difference, however, both the Caudalian and CAN disc models are suitable for reproducing the larger-scale observed structures in the magnetodisc field, as we shall see in the following sections. The main advantage of the Caudalian disc is that it also provides realistic spatial profiles of current and radial force arising from *self-consistent* global distributions of plasma.

### 3.2 Response of Magnetodisc to Solar Wind Pressure

In this section, we parametrise the effect of solar wind dynamic pressure by varying the magnetopause radius  $R_{MP}$  in our model calculations. In Fig. 13, we present model outputs calculated for two configurations; the first corresponds to strongly compressed

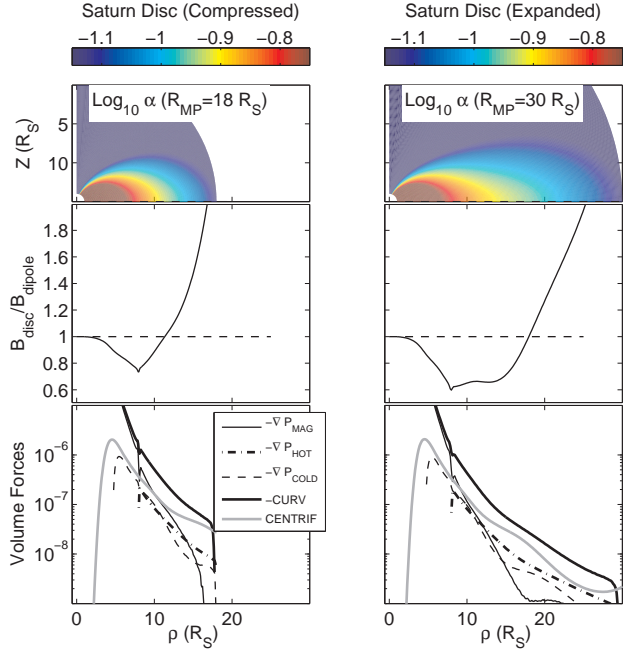


**Figure 13.** The left and right columns of plots correspond respectively to Saturn disc models calculated for compressed ( $R_{MP} = 18 R_S$ ) and expanded ( $R_{MP} = 25 R_S$ ) configurations. Top panels: The logarithm of magnetic potential  $\alpha$  is plotted on a colour scale for the labelled configurations. Middle panels: The equatorial ratio of total to dipole magnetic field strength is plotted for both magnetodisc configurations. The increased field strength of the compressed magnetodisc is apparent. Bottom panels: Equatorial profiles of normalised volume forces for the compressed and expanded models, labelled according to line style. We only plot the regions where the force profiles are positive on the logarithmic scale (as in Fig. 10, the negative of the curvature force is used here to demonstrate the balance between it and the other forces).

conditions for the Kronian magnetosphere with  $R_{MP} = 18 R_S$ , and the second is for a value  $R_{MP} = 30 R_S$  which is typical of the most expanded magnetospheric structures observed in the *Cassini* era (Achilleos et al. 2008; Arridge et al. 2006).

We commence our comparison of the compressed and expanded magnetodisc structures by considering the top panels of Fig. 13 which show contours of constant magnetic potential  $\alpha$ , equivalent to field line shapes. The region of strongly-radial field near the equatorial plane, as seen in the average model (§3.1), is also present in the expanded disc, particularly in the range  $\rho \sim 15\text{--}20 R_S$ . The compressed magnetodisc, on the other hand, displays field line shapes which are far less radially ‘stretched’ and which more closely resemble the geometry of a pure dipole (see Fig. 9). The colour scale of the upper panels in Fig. 13 indicates that both compressed and expanded models have similar levels of magnetic flux threading their entire equatorial planes; we therefore expect higher field strengths to be present in the compressed disc. The middle panels confirm that this is the case. Equatorial profiles of total magnetic field strength relative to that of the planetary dipole are shown as a function of  $\rho$ . Beyond  $\sim 5 R_S$ , the compressed disc model has a persistently stronger magnetic field than the expanded one. Around  $\sim 15 R_S$ , for example, the compressed field has reached a magnitude twice as large as the expanded configuration.

This behaviour of the field strength and geometry under

strongly-compressed conditions has important consequences for the ensuing magnetic forces which operate within the plasmadisc. In the bottom panels of Fig. 13, we plot equatorial profiles of the volume forces due to plasma pressure gradients, magnetic pressure gradient, magnetic curvature and centrifugal force. We follow the same convention as for Fig. 10, and show the negative curvature force, so that the principal regions of radially-inward curvature force and radially-outward other forces appear on the logarithmic scale as positive quantities.

The plots show that magnetic curvature is the principal, radially-inward force for both disc configurations. Closer inspections of the two curvature force profiles reveals a remarkable feature; the compressed model shows a stronger curvature force beyond  $\sim 8 R_S$ , whose ratio with respect to the expanded disc attains a maximum of  $\sim 1.4$  at  $\rho \sim 15\text{--}17 R_S$ . The compressed model is able to maintain a stronger curvature force via higher magnetic field strength, despite the increased radius of curvature of the local field line. This behaviour is qualitatively consistent with the study by Arridge et al. (2008b) mentioned in §1, which showed that the dayside magnetospheric field at Saturn only becomes significantly ‘disc-like’ under conditions of low solar wind dynamic pressure ( $R_{MP} > 23 R_S$ ).

Within the range of radial distances  $1 < \rho < 18 R_S$  covered by the compressed model's equatorial plane, there are also significant differences in magnetic pressure gradient and centrifugal force with respect to the expanded model. Firstly, the magnetic pressure within this distance range falls off with distance more gradually in the compressed disc. For both configurations, power-law fits to the magnetic pressure,  $P_{MAG} \propto \rho^{-2\chi}$ , were obtained for the interval  $10 < \rho < 15 R_S$ . The resulting indices were  $\chi = 2.80 \pm 0.14$  (compressed) and  $\chi = 3.27 \pm 0.10$  (expanded), revealing that the expanded model field falls off slightly more rapidly than a pure dipole  $\chi = 3$  in this region. However, a similar fit to the apparently more uniform part of the expanded field strength profile in the more distant magnetosphere  $20 < \rho < 25 R_S$  yielded  $\chi = 1.12 \pm 0.08$ . These results indicate that the compressed Kronian outer magnetosphere is likely to be characterised by field strength gradient similar to that of a dipole, while a more expanded configuration may be expected to exhibit a field with a more gradual decline, associated with values of the index  $\chi$  in the range 1–3. This predicted behaviour of the magnetospheric field suggests that observational studies of the relationship between magnetopause standoff distance and solar wind pressure may benefit from the assumption of a field strength index  $\chi$  which varies with  $R_{MP}$ , rather than the usually assumed fixed value (e.g. Achilleos et al. (2008); Arridge et al. (2006); Slavin et al. (1985)).

If we now turn our attention to the centrifugal force profiles in Fig. 13, a detailed inspection reveals that the compressed model exhibits a centrifugal force consistently stronger than that of the expanded disc for  $\sim 8 < \rho < 18 R_S$ , with the ratio of the two increasing monotonically to a value of  $\sim 2$ . This is a consequence of the higher cold plasma densities in the compressed model (at a given  $\rho$ , the ratio of centrifugal force between the two configurations is equivalent to the ratio of cold plasma density). In the region  $\sim 8 < \rho < 15 R_S$ , the plasma pressure gradients in the two models differ by less than 10 per cent. The increased centrifugal force of the compressed disc is thus balanced by an increased magnetic force (difference between magnetic curvature inward and magnetic pressure gradient outward). Interestingly, the region  $\sim 15 < \rho < 18 R_S$  near the compressed magnetopause is characterised by a change in sign of the magnetic pressure gra-

dient, which is required to maintain balance due to the curvature force decreasing more rapidly than the centrifugal force.

The region  $\sim 15 < \rho < 20 R_S$  for the expanded magnetodisc has force balance mainly determined by magnetic curvature and centrifugal effects as shown by Fig. 13. The same region, however, has a broad local maximum in centrifugal force nearly coincident with a minimum in magnetic pressure gradient. These features arise because of the corresponding local maximum of plasma angular velocity in the same region (Fig. 7), and the field geometry producing a relatively uniform region of field strength. In the more distant magnetosphere near  $\sim 23\text{--}27 R_S$  hot plasma pressure gradient becomes equal in importance to centrifugal force in maintaining force balance due to the declining density and angular velocity of the cold disc plasma. As for the case of the compressed disc, the magnetic pressure near the magnetopause in the expanded model begins to increase with distance in order to maintain force balance near the boundary.

### 3.3 Comparison of Model to Magnetic Field Observations

A comprehensive comparison of our magnetodisc model for Saturn with the vast field and plasma datasets from the *Cassini* spacecraft is beyond the scope of this paper. For the sake of a preliminary assessment of how well the model may be applied to spacecraft observations, we shall present in this section a comparison between the magnetodisc model field and magnetometer observations from the *Cassini* spacecraft from two quite different orbits. The first is the Revolution 3 (Rev 3) orbit lying entirely within Saturn's rotational equator, from the early part of the mission (February 2005) and the second is the highly-inclined rev 3 orbit from March 2007 which samples the entire vertical structure of the disc.

Fig. 14 depicts the information relevant for our comparison based on *Cassini* rev 3, covering a period of approximately four days in February 2005. The time axis is labelled in days since the beginning of Day of Year 44, or February 13. The bottom panel shows the position of *Cassini* as a function of time using the colour-coded  $\rho$  and  $Z$  cylindrical coordinates as well as the Saturn local time (SLT) in decimal hours. We see that this inbound pass of the orbit samples the magnetosphere at radial distances  $\rho \sim 4\text{--}31 R_S$ , the largest distance in this range corresponding to the indicated magnetopause crossing. The orbital segment for which  $\rho \gtrsim 8 R_S$  is situated at near-noon local times between  $\sim 10$  and  $14$  h (SLT). The entire orbit is also situated within or very close to the equatorial plane  $Z = 0$ . This region of space is thus appropriate for analysis with our model, which is representative of dayside conditions at Saturn and which uses a simplified formulation for the field due to magnetopause currents, based on an empirical model of the dayside equatorial field due to this source (§3.1).

The upper panels of Fig. 14 show the  $B_\rho$  and  $B_Z$  components of the magnetic field (black curve) observed by *Cassini* during the relevant time interval, in nT units, from which we have subtracted the components of the internal field model described by Dougherty et al. (2005). The plotted data thus represents the magnetic field due to the external sources of the current disc and magnetospheric boundaries. To analyse the  $B_Z$  observations, we chose two models. The first is the non-homogeneous part of our magnetodisc model (i.e. the total field model minus the planetary dipole term) with hot plasma index  $K_h = 2 \cdot 10^6 \text{ Pa m T}^{-1}$  (representing approximately average ring current activity at Saturn) and appropriate magnetopause radius  $R_{MP} = 30 R_S$ . The value for  $R_{MP}$  based on the magnetopause crossing location and the magnetopause model of Arridge et al. (2006) is  $28 R_S$  — the use of either

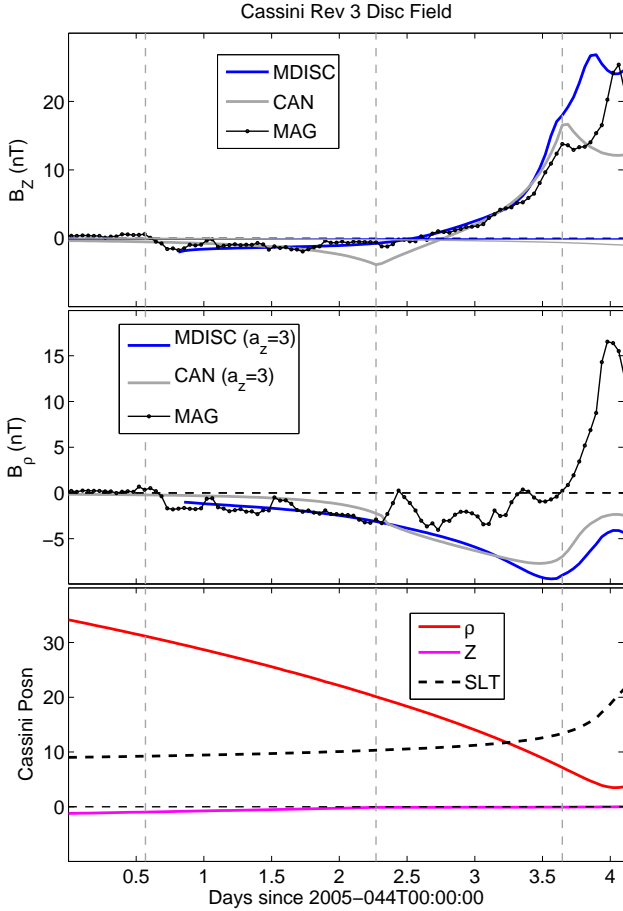


**Figure 14.** The top two panels show comparison between modified *Cassini* magnetometer data from the rev 3 orbit (‘MAG’) and models which employ the Connerney (‘CAN’) and Caudalian (‘MDISC’) discs, with parameters as described in the text. The thin coloured curves in the top panel represent the small contributions in the models from magnetopause and tail currents. Vertical ( $B_z$ ) and radial ( $B_\rho$ ) field components are shown as a function of time. The data are hourly averages and have had the internal field model described by Dougherty et al. (2005) subtracted. The middle panel uses a magnetic equator for the models which is displaced by  $3 R_S$  north of the planet’s rotational equator (without such a displacement, the models’ predicted values for  $B_\rho$  would be identically zero for this equatorial orbit). The bottom panel shows the spacecraft position as a function of time (cylindrical radial ( $\rho$ ) and vertical ( $Z$ ) distance, SLT). The vertical dashed lines indicate, from left to right, the positions of the last inbound magnetopause crossing, the outer edge of the CAN model disc ( $20 R_S$ ) and the inner edge of the same model ( $7 R_S$ ). The CAN disc parameters were taken from Bunce et al. (2007), who fit a non-displaced model to observations of  $B_z$ .

value did not significantly change the results. The  $B_z$  values shown by the blue curve were obtained by linear interpolation of the field values from our 2D model grid onto the spacecraft trajectory.

We also show, using grey curves, the predictions from the CAN model used by Bunce et al. (2007) to analyse these data. The parameters for this model are the azimuthal scale current per unit radial length  $I_0$ , the inner and outer edges of the annular model disc ( $a$  and  $b$ ) and the disc half width in the  $Z$  direction ( $D$ ). The parameter values we chose were the following, as determined by Bunce et al. (2007):  $\mu_0 I_0 = 53.3 \text{ nT}$ ,  $a = 7 R_S$ ,  $b = 20 R_S$ ,  $D = 2.5 R_S$ .

The thin blue and grey curves show the corresponding contributions from the magnetopause shielding field to the different disc

models. On the scale of the plot, the uniform shielding field of our model (see Fig. 8) has a barely discernible magnitude of  $0.09 \text{ nT}$ . As for our Caudalian model, the shielding field for the CAN model was assumed to lie entirely in the  $Z$  direction, but was computed using the following formula from Bunce et al. (2007):

$$B_z^{\text{MP}} = \frac{B_1(X - X_2) + B_2(X_1 - X)}{X_1 - X_2}. \quad (21)$$

This expression describes a shielding field which changes linearly with  $X$ , the spatial coordinate associated with the axis which lies along the intersection of the equatorial plane and the noon-midnight meridian ( $X$  positive towards the Sun). The parameter values  $B_1 = 0 \text{ nT}$  and  $B_2 = -1.11 \text{ nT}$  were chosen to fit the observed  $B_z$  values at the position of the magnetopause ( $X_1 = 23.36 R_S$ ) and the nightside location with the minimum value of  $X$  ( $X_2 = -6.17 R_S$ ). It is evident that the shielding field for both models makes only a very minor contribution to the total predicted field except, for the CAN model, in the region adjacent to the magnetopause.

Structure at a variety of timescales is evident in the observations. The global nature of the disc models implies that they are suitable for analysing the largest scales, of the order half a day in time or a few planetary radii in  $\rho$ . If we firstly consider the  $B_z$  field, both models reasonably reproduce the overall trend seen in the observations. Near the location of the outer edge of the CAN model (vertical line at  $\sim 2.3$  days), we see that this model predicts a relatively sharp minimum in  $B_z$  due to the truncated nature of its current disc. The Caudalian disc with its extended current sheet makes a smoother transition in  $B_z$  through this region in better agreement with the observations. On the other hand, near the location of the inner edge of the CAN model (vertical line at  $\sim 3.7$  days) the local peak in  $B_z$  displayed by this model fits the data more closely than the Caudalian disc, which rises to values more than twice that of the data within this inner region. This suggests a need for more accurate plasma inputs in the region  $\rho \lesssim 5 R_S$  of our model, as discussed in §2.3.1 and §2.3.2. The local peak in the  $B_z$  data near  $\sim 4$  days is most likely a signature of the ‘camshaft’ field at Saturn. This is a quasi-periodic modulation seen in the magnetic field whose physical origin remains to be unambiguously identified, but appears to be linked with field-aligned, azimuthally-modulated magnetospheric currents flowing between the ionosphere and plasmasphere (e.g. Southwood & Kivelson (2007); Provan et al. (2009)). We shall return to this aspect when we consider the high-latitude observations.

Both disc models fail to agree with the  $B_\rho$  data in Fig. 14. This is because they have a north-south hemispherical symmetry, which by definition requires  $B_\rho = 0$  within the equatorial plane. The fact that *Cassini* observes a significantly non-zero  $B_\rho$  in rev 3 and many other equatorial orbits has been suggested to be the result of a non-planar plasmasphere structure; in particular, the bowl-shaped current sheet model explored by Arridge et al. (2008a) provides an explanation for these observations. Such a sheet morphology would be expected to arise in a magnetosphere where the planetary dipole is significantly non-orthogonal with respect to the upstream solar wind flow direction, as was the case during rev 3, where the angle between these two directions was  $\sim 70^\circ$  (the northern magnetic pole being tilted away from the Sun). As a first, albeit crude, approximation to the ensuing field geometry, the model  $B_\rho$  values shown are those corresponding to model plasmaspheres which have been displaced by a distance of  $3 R_S$  north of Saturn’s rotational equator. In the region between the magnetopause boundary and the neighbourhood of the outer edge of the CAN disc, both

models and data are in reasonable agreement, confirming that a displaced planar disc is a useful representation of the local effects of the more realistic bowl-like shape. As we proceed closer to the planet along the spacecraft orbit towards the inner CAN disc edge, the observed  $B_\rho$  decreases in magnitude, consistent with the magnetic equator of the plasmadisc becoming aligned with the rotational equator; the displaced model values, unsurprisingly, do not fit the data in this region. We see a local peak in the observed  $B_\rho$  near  $4 R_S$  corresponding to the similar feature in  $B_Z$  which probably arises from the ‘camshaft’ field (e.g. examining different orbits, Southwood & Kivelson (2007) report camshaft amplitudes of the order of several nT in this region).

In the panels of Fig. 15, we plot magnetic field components and spacecraft position as a function of time using the same scheme and conventions as Fig. 14. The time interval in question covers about nine days from the beginning of March 21, 2007 which correspond to the closest approach to Saturn and outbound segment of the rev 3 orbit. The  $Z$  co-ordinate trace in spacecraft position shows that during this time *Cassini* probed regions up to  $15 R_S$  from the equatorial plane, and the spacecraft latitude reached magnitudes of  $\sim 60^\circ$ . In addition, at the time intervals near 6.5 and 10 days, the spacecraft traversed the full extent in  $Z$  through the current sheet, a structure with typical vertical length scales of a few  $R_S$ . From the §3.1 discussion, typical length scales along the  $\rho$  co-ordinate for the cold disc plasma are  $\sim 1\text{--}5 R_S$ , which therefore provide an upper bound for the length scale along  $Z$ . rev 3 thus provides a very different view of the magnetosphere compared to the equatorial pass of rev 3 and hence a good means of further testing the suitability of the disc models for magnetic analyses.

We shall consider firstly the  $B_Z$  data and model predictions in the top panel of Fig. 15. As for rev 3, structure in the magnetic field on a variety of time scales is seen; in particular, the quasi-periodic ( $\sim 10.75$  hr) camshaft signal in  $B_Z$  is clearly evident with typical amplitudes of the order 1 nT. We shall return to this feature presently after discussing the larger-scale features in the field profile. The Caudalian and CAN disc models used for comparison purposes are shown as thick blue and grey curves. We chose the following parameters for the CAN disc, obtained from a least-squares fit to the combination of both observed field components as displayed in the Figure:  $\mu_0 I_0 = 40$  nT,  $a = 6.6 R_S$ ,  $b = 18.6 R_S$ ,  $D = 3.2 R_S$ . The thin grey curve shows the shielding field profile used in the CAN model, computed using the following parameters for Eq. (21):  $B_1 = 0.5$  nT,  $B_2 = 1.5$  nT,  $X_1 = 15 R_S$ ,  $X_2 = -14 R_S$ . The thin blue curve shows a modified version of the Caudalian disc, which we describe in more detail later in this section.

The location of the outbound magnetopause crossing at  $(\rho, Z) = (26.8, 17.3) R_S$  corresponds to a subsolar standoff distance  $R_{MP} = 24 R_S$ , using the axisymmetric magnetopause model of Arridge et al. (2006). However, we found that the Kronian disc model with a somewhat larger magnetopause radius  $R_{MP} = 30 R_S$  gave significantly better agreement with the observations, and it is the field profiles for this more expanded model which we have displayed. Since the magnetopause crossing was at a relatively high altitude  $Z$  above the equator, this finding may indicate that the magnetopause of Saturn exhibits polar flattening, although evidence for this requires further studies of similar mid- to high-latitude boundary crossings.

For the interval spanning closest approach until the outbound magnetopause crossing, both disc models reproduce the large-scale trend in  $B_Z$  from the magnetometry. The Caudalian disc predicts a mean field about 1 nT weaker than that observed in the time in-

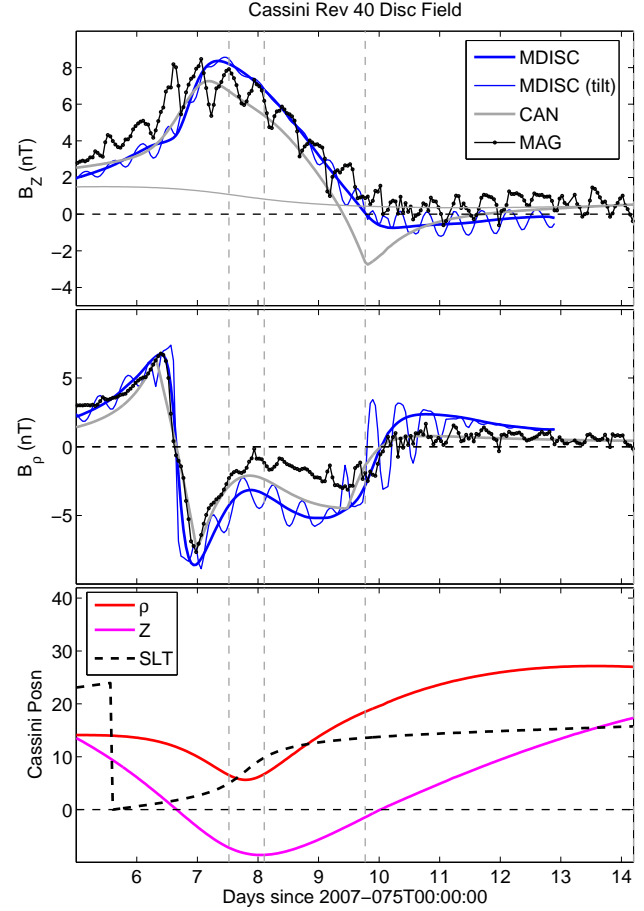


**Figure 15.** Plots analogous to Fig. 14 for the *Cassini* rev 3 orbit. Predictions for a rotating disc whose axis is tilted at  $10^\circ$  to that of the planet’s rotation axis are also shown (‘MDISC (tilt)’). The vertical dashed lines indicate the positions of the inner ( $6.6 R_S$ ) and outer ( $18.6 R_S$ ) radii of the CAN disc, whose parameters have been chosen to best fit the  $B_\rho$  data (see text). The time axis is truncated on the right at the first outbound magnetopause crossing.

terval after 10 days. This feature suggests that a positive shielding field, similar to that employed for the CAN model, may be a more realistic choice for this pass than the uniform negative value  $-0.09$  nT used in our model (see Fig. 8). The camshaft signal in  $B_Z$  is observed throughout this orbit. This field source, when added to the planetary dipole, has been suggested to be equivalent to that of a tilted, rotating dipole in the outer magnetosphere  $\rho \gtrsim 15 R_S$  (Southwood & Kivelson 2007). In this picture, we would expect the magnetic equator of the outer Kronian plasmadisc to also be tilted relative to the rotational equator. As a preliminary exploration of this concept, we have plotted in Fig. 15 a thin blue curve showing the field profiles associated with a tilted, rotating plasmadisc. We computed these profiles by simply taking the original magnetodisc model and transforming it to a co-ordinate system where the model’s axis of cylindrical symmetry is tilted at an angle of  $10^\circ$  with respect to the planet’s rotation axis (the latter now being defined as the  $Z$  direction in accordance with the data). The orientation of the model symmetry axis was also allowed to vary with time such that the azimuthal angle of its projection onto the rotational equator corresponded to a regular rotation with a period of 10.75 h. We note that the observed camshaft signal does not have a fixed period, but one which may drift in value by the order of a

minute over time scales of the order of a year, as revealed by its radio signature, e.g. Kurth et al. (2007, 2008).

While the phase and amplitude of the tilted disc  $B_Z$  fluctuations match the data on the outbound pass reasonably well for  $\rho \gtrsim 10 R_S$ , they rapidly diminish inside this region. This behaviour is a result of the magnetic field geometry due to the current disc alone, as illustrated in Fig. 16. In this Figure, we show magnetic field line shapes, contours of  $B_Z$  and contours of  $B_\rho$  for the contribution to the model magnetic field from the plasmadisc currents alone. The field line shapes indicate a solenoid-like geometry for this source. All panels in Fig. 16 also show the rev 3 trajectory of *Cassini* plotted on the  $(\rho, Z)$  co-ordinate plane. The thick black arcs show the effective regions of the model field sampled by two fixed observers as a result of the global motion of the rotating, tilted Caudalian disc which we have described above. The first of these fictitious observers is located at the closest-approach point of the orbit and the other at the outbound current sheet crossing. We see that the first observer experiences very little change in  $B_Z$  due to a rotating, tilted disc since the corresponding excursion over one period is almost parallel to the constant  $B_Z$  contour. On the other hand, the observer at the outbound current sheet crossing can expect to see a change in  $B_Z$  as the locus of their excursion would cut across the local  $B_Z$  contour shapes. This picture of course explains the behaviour of the model  $B_Z$  fluctuations in Fig. 15, but does not account for the persistent observed camshaft fluctuations near closest approach. Southwood & Kivelson (2007) studied the phase relations between the camshaft field components and concluded that the equivalent rotating, tilted dipole model is appropriate only beyond  $\rho \sim 15 R_S$  where the field-aligned currents associated with this phenomenon are flowing. Our simple rotating, tilted disc calculations are therefore consistent with their conclusion.

Let us now consider the  $B_\rho$  observations in Fig. 15. The two current sheet crossings are characterised by the relatively rapid change in sign of the  $B_\rho$  field as we cross between regions of outward- and inward-pointing field (see also Fig. 16, top panel). Both disc models mimic this behaviour; however, our Caudalian disc model shows smoother transitions in field through the current sheet compared to the CAN model's sharper peaks at local maxima in  $|B_\rho|$  near the current sheet crossings. This difference is due to the CAN annular disc geometry where the current source is confined within a region having distinct boundaries in space, in contrast with the Caudalian model where disc plasma does not suddenly disappear outside a given region, but is globally distributed according to the force balance condition. The bottom panel of Fig. 16 explains why the model fluctuations in  $B_\rho$  due to the rotating, tilted disc have larger amplitude near current sheet crossings, where the observer's locus cuts through many contours in  $B_\rho$ , compared to the position near closest approach, where the intercepted contours are fewer in number. The magnetometer data, however, show camshaft  $B_\rho$  fluctuations near the current sheet crossings and at smaller radial distances which are either negligible or very weak compared to the model. As for the  $B_Z$  comparison, a rotating, tilted disc only seems appropriate for reproducing outer magnetospheric behaviour over the time scales of spacecraft orbits such as those we have considered. The CAN model lies closer to the observed  $B_\rho$  values near closest approach. However, this region of the orbit samples relatively high latitudes up to  $60^\circ$  where more realistic treatments of the magnetopause and tail would be required in models of this nature, which were originally devised for low-latitude and equatorial analyses.

### Field Line Geometry: Disc Source $R_{MP}=30$

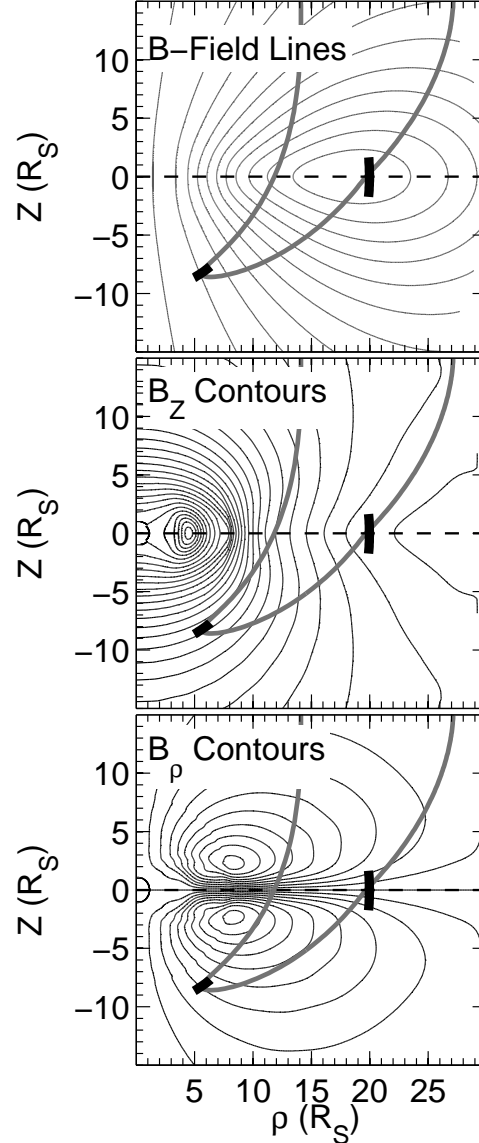


**Figure 16.** Upper panel: Magnetic field line shapes (thin grey lines) are shown for the corresponding field due to the model current disc (excluding planetary dipole) with magnetopause radius  $R_{MP} = 30 R_S$ . The *Cassini* trajectory for rev 3 in the same  $(\rho, Z)$  co-ordinate plane as the model is shown as a thick grey curve. The very thick black arcs indicate excursions through the model field during one period of the rotating, tilted disc configuration (see text) for observers situated near the orbit's closest approach to Saturn and outbound current sheet crossing; Middle panel: Equally-spaced contours of constant vertical magnetic field  $B_Z$  corresponding to the same model geometry as the top panel. The maximum strength for  $B_Z$  is situated at the smallest closed contour, near  $\rho = 5$  along the equator. The rev 3 orbit and rotating model excursions are depicted as a thick grey curve and thick black arcs, as for the top panel; Bottom panel: Equally-spaced contours of constant radial magnetic field  $B_\rho$  corresponding to the same geometry as the top panel. Local maxima in the magnitude of  $B_\rho$  are situated at the smallest closed contours, near the regions  $\rho = 8-9$  and  $Z = \pm 2-3$ . The rev 3 orbit and rotating model excursions are depicted as a thick grey curve and thick black arcs, as for the top panel;

#### 4 SUMMARY AND DISCUSSION

We have introduced a new model for Saturn's magnetodisc, based on an original formalism by Caudal (1986). The model formalism is based on the magnetostatic solution for an Euler potential consistent with global balance between plasma pressure gradient, centrifugal force and magnetic force ( $\mathbf{J} \times \mathbf{B}$ ) in a cylindrically symmetric system. Such an approach has the advantage of being able to predict a self-consistent system of plasma properties, magnetospheric azimuthal currents and magnetic field. The equatorial boundary condition for the model was provided by observations from the *Cassini* spacecraft of hot and cold plasma pressure, and cold plasma density and temperature (§2.3 and subsections). In order to formulate a model with realistic global behaviour, we adopted relatively simple functional forms for these physical parameters. In this context, the unit flux tube volume concept was applied, following Caudal (1986), in order to compute global distributions of plasma whose density and pressure would respond appropriately to different magnetospheric radii, according to the behaviour expected of a 'frozen-in' plasma. The empirical fits to hot plasma pressure, cold plasma composition and cold plasma temperature by Sergis et al. (2007, 2009); Wilson et al. (2008) were employed in order to achieve a reasonable representation for the model equator of average magnetospheric conditions at Saturn. We also used a polynomial fit to the data by Kane et al. (2008); Wilson et al. (2008) for plasma angular velocity.

Before presenting the outputs from the full model, we considered a simple toy model emphasising the largest angular scales of the magnetic potential for a homogeneous disc, characterised by constant plasma  $\beta$ , constant plasma scale length  $\ell$  and full corotation with the parent planet. This simple model was used to show the influence on magnetic field geometry to be expected when a rotating plasmasdisc is added to a planetary dipole. In particular, hot plasma pressure generally inflates outer magnetospheric flux tubes to greater radial distances while the centrifugal confinement of the rotating cold plasma towards the equator gives rise to inflated, relatively oblate field lines.

This zeroth-order behaviour was consistent with our full model for Saturn's magnetodisc under average internal (ring current activity) and external (solar wind) conditions. Our consideration of this baseline model, for which magnetopause radius  $R_{MP} = 25 R_S$  confirmed the radial 'stretching' of the unperturbed dipolar field lines as a result of the currents flowing mainly in the equatorial plasmasdisc. The corresponding equatorial field strength in the model shows a region where it falls below the unperturbed dipole value for distances  $\sim 5\text{--}15 R_S$  and exceeds the dipole value beyond this range, also displaying a comparatively more gradual decrease with radial distance in the outer magnetosphere. All of these features are general characteristics which arise from adding the solenoid-like magnetic field of the disc (ring) current alone to the planetary dipole.

Examination of the equatorial radial forces in the average Kronian disc model revealed that, for distances beyond  $\sim 15 R_S$ , the principal forces determining disc structure are the magnetic curvature and centrifugal forces. This characteristic distance is consistent with the simple formula for the 'transition distance'  $\rho_T$  between pressure- and centrifugal-dominated structure which arose from the zeroth-order disc treatment. This formula reveals the conditions under which  $\rho_T$  is most likely to exceed magnetopause radius, and consequently the plasmasdisc can never have a force balance dominated by centrifugal force. The relevant conditions are: (i) Hot plasma  $\beta$  is very high compared to the cold plasma (i.e.

thermal energy is large compared to rotational kinetic energy); (ii) Plasma angular velocity is adequately low; or (iii) For a given temperature of cold plasma, its density is small (such that the quantity  $\ell^2/\beta_c$  becomes very large).

Consideration of the equatorial, azimuthal current density  $J_\phi$  in the average Kronian disc model revealed that centrifugal inertial current was the primary contribution for distances beyond  $\sim 13 R_S$ . For the region  $\sim 8\text{--}12 R_S$ , hot plasma and centrifugal current were predicted to be comparable. However, a further exploration of more active ring current states (future study) is likely to show that this interval in distance will expand, and the hot plasma current intensify, as the hot plasma index  $K_h$  is increased beyond values appropriate for average conditions at Saturn.

A comparison of the azimuthal current profiles between the average Saturn disc model and a reproduction of the Jovian magnetodisc by Caudal (1986) (for which  $R_{MP} = 80 R_J$ ) was also revealing. In particular, the calculations confirmed that the increased  $\beta_h/\beta_c$  ratio at Jupiter endows this planet's magnetosphere with equatorial azimuthal current dominantly due to hot plasma pressure beyond a distance  $\sim 30 R_J$ . Within  $\sim 20\text{--}30 R_J$ , the centrifugal and hot plasma currents are of similar magnitude.

The normalised (dimensionless) quantities adopted in our model enabled us to make an important comparison between the strength of the azimuthal current density at Saturn and Jupiter. The values of normalised equatorial  $J_\phi$  at Saturn, according to our calculations, are expected to exceed those at Jupiter by factors of  $\sim 5$  within the distance range  $\sim 5\text{--}16$  planetary radii. The implication of this result is that, while the absolute strength of the Kronian currents is far weaker than their Jovian counterparts, the *relative* perturbation to Saturn's internal field in this distance range due to the disc current would exceed that at Jupiter.

In §3.2 we examined the response of the Saturn disc model to conditions of compressed ( $R_{MP} = 18 R_S$ ) and expanded ( $R_{MP} = 30 R_S$ ) magnetospheric configuration. Both models generally showed centrifugally-dominated force balance beyond  $\sim 15 R_S$ , although the expanded disc shows comparable centrifugal force and hot plasma pressure gradient near  $\sim 25 R_S$  due to the decline in cold plasma angular velocity. Interestingly, the compressed disc is able to maintain a similar or stronger curvature force than the expanded one, despite having nearly dipole-shaped field lines: this property is a consequence of the higher field strengths attained in the compressed magnetospheric state. Around  $\sim 15 R_S$ , for example, the compressed model's equatorial field already reaches a magnitude twice as large as the expanded configuration. Consideration of the gradients in magnetic pressure in the compressed and expanded disc models indicated that the index  $\chi = -\frac{\rho}{B} \frac{dB}{d\rho}$ , which characterises the relative change in field strength  $B$  per relative change in radial distance  $\rho$ , is likely to vary as a function of magnetopause standoff distance. This dependence recommends the corresponding use of a variable  $\chi$  in future observational studies of the response of Saturn's magnetopause boundary to changing solar wind conditions.

Finally, in §3.3, we presented model calculations for a Kronian disc model with  $R_{MP} = 30 R_S$  and average hot plasma index. We compared our model predictions for vertical ( $B_z$ ) and radial ( $B_\rho$ ) field components with magnetometer data from two of the orbits of the *Cassini* spacecraft's prime mission. We also presented model calculations for appropriate CAN annular disc models (Connerney et al. 1981) as part of this comparison. In general, both the Caudalian and CAN disc model were able to account for the general large-scale trends seen in the data-derived magnetic field due to the magnetodisc current alone. However, certain dis-

crepancies between the models and the observations point to a need to use non-planar disc geometries in more detailed studies. The first of these discrepancies is the non-zero radial field observed by *Cassini* during the rev 3 orbit considered herein, which cannot be explained by a disc field with north-south hemispheric symmetry. An observational study by Arridge et al. (2008a) for many equatorial orbits revealed that this is a repeatable signature, and is most likely associated with a bowl-shaped current sheet.

The second important discrepancy between our model calculations and the magnetometry is the presence of observed quasi-periodic fluctuations in the field, known as the camshaft signal. While our rotating, tilted disc model was able to qualitatively reproduce similar field fluctuations in the outer magnetosphere ( $\rho \gtrsim 15\text{--}20 R_S$ ), it was clearly not capable of explaining the observed behaviour of the camshaft signal for regions closer to the planet. A general advantage of the Caudalian disc model in the context of data interpretation is that its more realistic plasma distribution yields smoother predicted changes in field orientation for spacecraft passes through the current sheet. The CAN model predicts sharp peaks in field components during such transitions due to its assumption of an annular geometry with definitive boundaries for the current-carrying region; it also shows similar abrupt changes in field for the regions near the assumed inner and outer edges where the current region is truncated. The discussion in §3.1 revealed that the force balance used to derive the Caudalian disc structure also results in a fall-off in magnetospheric current density more rapid than the  $1/\rho$  law assumed in the CAN model.

The Caudalian magnetodisc for Saturn represents a useful first model for pursuing studies of the plasmadisc structure, azimuthal current and magnetospheric field, along the lines that we have presented in this paper. While these initial studies have revealed some interesting features of disc structure and currents at Saturn, particularly when compared to the Jovian system, they also highlight some important future directions for work involving this model, such as the following:

(i) Improved determinations of plasma moments should be incorporated into the structure of the model, in order to provide more accurate depictions of the global plasma conditions.

(ii) Investigation of the influence of hot plasma pressure on magnetodisc structure. Our initial study has revealed that it plays a potentially important role in determining the general structure of the magnetodisc field and the extent of the magnetospheric region where the electric current density  $J_\phi$  is dominantly determined by energetic particle motions, rather than the inertial current associated with centrifugal force acting on the cold population.

(iii) An extension of our preliminary study of solar wind influence on disc structure to additional magnetopause radii and global characterisations of internal plasma energy and content. The self-consistent response of plasma angular velocity to magnetospheric compression could also play a potentially important role here.

(iv) Further analyses of *Cassini* field and plasma data. The spacecraft has thus far completed more than 100 orbits of Saturn. Such a vast dataset will require much time to exploit. A suitable use for our model with regard to the field and particle data would be a modelling study of selected orbits using input plasma moments acquired during those orbits, rather than a ‘global approximation’ to these conditions. The model outputs would thus reflect conditions most appropriate for the orbits in question. Such calculations would be of use, for example, to teams who aim to derive magnetospheric particle fluxes and current densities directly from *in situ* measurements.

## ACKNOWLEDGEMENTS

The authors acknowledge the continued support and collaboration of the *Cassini* magnetometer (MAG), plasma spectrometer (CAPS) and magnetospheric imager teams (MIMI). CSA was supported for part of this work by an STFC rolling grant at MSSL. PG was supported for part of this work by an STFC rolling grant at UCL Physics and Astronomy. NA wishes to thank Nick Sergis, Cesar Bertucci and Stephanie Kellett for useful discussions.

## REFERENCES

- Achilleos N., Arridge C. S., Bertucci C., Jackman C. M., Dougherty M. K., Khurana K. K., Russell C. T., 2008, *J. Geophys. Res.*, **113**, A11209
- Alexeev I. I., Belenkaya E. S., 2005, *Ann. Geophys.*, **23**, 809
- Alexeev I. I., Kalegaev V. V., Belenkaya E. S., Bobrovnikov S. Y., Bunce E. J., Cowley S. W. H., Nichols J. D., 2006, *Geophys. Res. Lett.*, **33**, 8101
- Arridge C. S., Achilleos N., Dougherty M. K., Khurana K. K., Russell C. T., 2006, *J. Geophys. Res.*, **111**, A11227
- Arridge C. S., Khurana K. K., Russell C. T., Southwood D. J., Achilleos N., Dougherty M. K., Coates A. J., Leinweber H. K., 2008a, *J. Geophys. Res.*, **113**, 8217
- Arridge C. S., Russell C. T., Khurana K. K., Achilleos N., André N., Rymer A. M., Dougherty M. K., Coates A. J., 2007, *Geophys. Res. Lett.*, **34**, L09108
- Arridge C. S., Russell C. T., Khurana K. K., Achilleos N., Cowley S. W. H., Dougherty M. K., Southwood D. J., Bunce E. J., 2008b, *J. Geophys. Res.*, **113**, 4214
- Bagenal F., Sullivan J. D., 1981, *J. Geophys. Res.*, **86**, 8447
- Bunce E. J., Cowley S. W. H., Alexeev I. I., Arridge C. S., Dougherty M. K., Nichols J. D., Russell C. T., 2007, *J. Geophys. Res.*, **112**, 10202
- Caudal G., 1986, *J. Geophys. Res.*, **91**, 4201
- Caudal G., Connerney J. E. P., 1989, *J. Geophys. Res.*, **94**, 15055
- Connerney J. E. P., Acuna M. H., Ness N. F., 1981, *Nature*, **292**, 724
- , 1983, *J. Geophys. Res.*, **88**, 8779
- Dialynas K., Krimigis S. M., Mitchell D. G., Hamilton D. C., Krupp N., Brandt P. C., 2009, *J. Geophys. Res.*, **114**
- Dougherty M. K., Achilleos N., André N., Arridge C. S., Balogh A., Bertucci C., Burton M. E., Cowley S. W. H., Erdos G., Giampieri G., Glassmeier K.-H., Khurana K. K., Leisner J., Neubauer F. M., Russell C. T., Smith E. J., Southwood D. J., Tsurutani B. T., 2005, *Science*, **307**, 1266
- Dougherty M. K., Kellock S., Southwood D. J., Balogh A., Smith E. J., Tsurutani B. T., Gerlach B., Glassmeier K.-H., Gleim F., Russell C. T., Erdos G., Neubauer F. M., Cowley S. W. H., 2004, *Space Science Reviews*, **114**, 331
- Giampieri G., Dougherty M., 2004, *Ann. Geophys.*, **22**, 653
- Gledhill J. A., 1967, *Nature*, **214**, 155
- Gleeson L. J., Axford W. I., 1976, *J. Geophys. Res.*, **81**, 3403
- Goertz C. K., Randall B. A., Thomsen M. F., Jones D. E., Smith E. J., 1976, *J. Geophys. Res.*, **81**, 3393
- Hill T. W., Carbary J. F., 1978, *J. Geophys. Res.*, **83**, 5745
- Kane M., Mitchell D. G., Carbary J. F., Krimigis S. M., Crary F. J., 2008, *Geophys. Res. Lett.*, **35**, 4102
- Khurana K. K., Arridge C. S., Schwarzl H., Dougherty M. K., 2006, “AGU Spring Meeting Abstracts”, P44:A01
- Kivelson M. G., Khurana K. K., Russell C. T., Walker R. J., Coleman P. J., Coroniti F. V., Green J., Joy S., McPherron R. L.,

- Polanskey C., Southwood D. J., Bennett L., Warnecke J., Hudleston D. E., 1997, *Adv. Space Res.*, 20, 193
- Kivelson M. G., Southwood D. J., 2005, *J. Geophys. Res.*, 110, A12209
- Krimigis S. M., Carbary J. F., Keath E. P., Bostrom C. O., Ax-  
ford W. I., Gloeckler G., Lanzerotti L. J., Armstrong T. P., 1981,  
*J. Geophys. Res.*, 86, 8227
- Krimigis S. M., Mitchell D. G., Hamilton D. C., Livi S., Dan-  
douras J., Jaskulek S., Armstrong T. P., Boldt J. D., Cheng A. F.,  
Gloeckler G., Hayes J. R., Hsieh K. C., Ip W.-H., Keath E. P.,  
Kirsch E., Krupp N., Lanzerotti L. J., Lundgren R., Mauk B. H.,  
McEntire R. W., Roelof E. C., Schlemm C. E., Tossman B. E.,  
Wilken B., Williams D. J., 2004, *Space Science Reviews*, 114,  
233
- Krimigis S. M., Sergis N., Mitchell D. G., Hamilton D. C., Krupp  
N., 2007, *Nature*, 450, 1050
- Kurth W. S., Averkamp T. F., et al., 2008, *J. Geophys. Res.*, 113,  
A05222
- Kurth W. S., Lecacheux A., et al., 2007, *Geophys. Res. Lett.*, 34,  
L02201
- Lackner K., 1970, *J. Geophys. Res.*, 75, 3180
- McAndrews H., Thomsen M., Arridge C., Jackman C., Wilson  
R., Henderson M., Tokar R., Khurana K., Sittler E., Coates A.,  
Dougherty M., 2009, *Planet. Space Sci.*, (in press)
- Provan G., Andrews D. J., Arridge C. S., Coates A. J., Cowley  
S. W. H., Milan S. E., Dougherty M. K., Wright D. M., 2009,  
*J. Geophys. Res.*, 114, A02225
- Richardson J. D., 1998, *Reviews of Geophysics*, 36, 501
- Sergis N., Krimigis S. M., Mitchell D. G., Hamilton D. C., Krupp  
N., Mauk B. H., Roelof E. C., Dougherty M. K., 2009, *J. Geo-  
phys. Res.*, 114, A02214
- Sergis N., Krimigis S. M., Mitchell D. G., Hamilton D. C., Krupp  
N., Mauk B. M., Roelof E. C., Dougherty M., 2007, *GRL*, 34,  
L09102
- Slavin J. A., Smith E. J., Spreiter J. R., Stahara S. S., 1985, *J. Geo-  
phys. Res.*, 90, 6275
- Smith E. J., Davis Jr. L., Jones D. E., Coleman Jr. P. J., Colburn  
D. S., Dyal P., Sonett C. P., 1975, *Science*, 188, 451
- Smith E. J., Davis Jr. L., Jones D. E., Coleman Jr. P. J., Colburn  
D. S., Dyal P., Sonett C. P., Frandsen A. M. A., 1974, *J. Geo-  
phys. Res.*, 79, 3501
- Southwood D. J., Kivelson M. G., 2007, *J. Geophys. Res.*, 112,  
A12222
- Sozou C., Windle D. W., 1970, *Planet. Space Sci.*, 18, 699
- Vasyliūnas V. M., 2008, *AnnGeo*, 26, 1341
- Wilson R. J., Tokar R. L., Henderson M. G., Hill T. W., Thomsen  
M. F., Pontius D. H., 2008, *J. Geophys. Res.*, 113, A12218
- Young D. T., Berthelier J. J., Blanc M., Burch J. L., Coates A. J.,  
Goldstein R., Grande M., Hill T. W., Johnson R. E., Kelha V.,  
McComas D. J., Sittler E. C., Svenes K. R., Szegő K., Tanskane-  
nen P., Ahola K., Anderson D., Bakshi S., Baragiola R. A., Bar-  
raclough B. L., Black R. K., Bolton S., Booker T., Bowman R.,  
Casey P., Crary F. J., Delapp D., Dirks G., Eaker N., Funsten H.,  
Furman J. D., Gosling J. T., Hannula H., Holmlund C., Huomo  
H., Illiano J. M., Jensen P., Johnson M. A., Linder D. R., Lun-  
tama T., Maurice S., McCabe K. P., Mursula K., Narheim B. T.,  
Nordholt J. E., Preece A., Rudzki J., Ruitberg A., Smith K., Sza-  
lai S., Thomsen M. F., Viherkanto K., Vilppola J., Vollmer T.,  
Wahl T. E., Wüest M., Ylikorpi T., Zinsmeyer C., 2004, *Space  
Science Reviews*, 114, 1

## APPENDIX A: SOLUTIONS FOR THE MAGNETODISC POTENTIAL

This Appendix describes the derivation of the solution for the mag-  
netic potential of an axisymmetric plasma distribution given in ar-  
ticles by Caudal (1986) and Lackner (1970). The potential in ques-  
tion is denoted by  $\alpha$  and is actually one of two Euler potentials  
from which the magnetic field  $\mathbf{B}$  may be derived

$$\mathbf{B} = \nabla\alpha \times \nabla\beta, \quad (\text{A1})$$

where  $\alpha$  is a function of radial distance  $r$  and cosine of colatitude  
 $\mu = \cos\theta$ . The function  $\beta$  depends only on azimuthal angle  $\phi$ :  
 $\beta = a\phi$  with  $a$  being the planetary radius. Note that many pairs of  
Euler potentials can be associated with a particular magnetic field,  
however this particular choice separates the azimuthal and merid-  
ional dependencies. In effect, these equations tell us that an indi-  
vidual magnetic field line can be thought of as the line of intersec-  
tion of a surface of constant  $\alpha$  (which will resemble a 'doughnut-  
shaped' shell) and a plane of constant  $\beta$  (which is simply the merid-  
ional plane with azimuth  $\phi$ ).

Let us now consider the differential equation for the merid-  
ional Euler potential  $\alpha$  given by Caudal (1986) (we shall use the  
dimensionless system of co-ordinates described in this paper):

$$\frac{\partial^2\alpha}{\partial r^2} + \frac{1-\mu^2}{r^2} \frac{\partial^2\alpha}{\partial \mu^2} = -g(r, \mu, \alpha). \quad (\text{A2})$$

In Eq. (A2), the function  $g$  represents a source term describ-  
ing a distribution of external plasma and currents which must be  
specified *a priori*. Note that  $g$  requires knowledge of  $\alpha$  as well —  
the function we are trying to solve for. Caudal (1986) and Lackner  
(1970) solve this problem through an iterative approach. One starts  
with an initial 'guess'  $\alpha_0$  for the functional form of  $\alpha$ .  $\alpha_0$  is then  
used to evaluate  $g$ , and then Eq. (A2) is solved to give an updated  
solution  $\alpha_1$ .  $\alpha_1$  is then used in the next iteration to re-evaluate  $g$   
and to update the solution again. The process is repeated until con-  
vergence: in practice, one usually stops when the maximum rela-  
tive difference between successive iterations falls below some user-  
defined tolerance.

A reasonable first guess for  $\alpha$  is the planetary dipole potential

$$\alpha_{\text{dip}}(r, \mu) = \frac{1-\mu^2}{r}. \quad (\text{A3})$$

$\alpha_{\text{dip}}$  is a homogeneous solution of Eq. (A2) (i.e. a solution for  
the case where the source term is identically zero). However, it is  
not the only homogeneous solution. Homogeneous solutions are  
a good starting point for finding *particular* solutions (i.e. when  
the source term is non-zero). We may obtain the general form of  
the homogeneous solution by using the property of separability i.e.  
 $\alpha(r, \mu) = \alpha_r(r)\alpha_\theta(\mu)$  is the product of two single-variable func-  
tions as stated previously. Substituting this into Eq. (A2) we can  
show that

$$\frac{r^2}{\alpha_r} \frac{d^2\alpha_r}{dr^2} + \frac{1-\mu^2}{\alpha_\theta} \frac{d^2\alpha_\theta}{d\mu^2} = 0. \quad (\text{A4})$$

Now if we fix the value of  $r$ , we would expect the left-hand  
term in this equation (a function of  $r$  only) to be a constant. How-  
ever the equation tells us that this constant is independent of what-  
ever value of  $\mu$  we use to evaluate the right-hand term. It follows  
that the right-hand term, regardless of the value of  $\mu$ , must be a  
constant. A similar argument, keeping  $\mu$  fixed, reveals that the left-  
hand term, for all values of  $r$ , must also be equal to a constant. If the  
constant takes on special values, derivable from an integer  $n \geq 0$ ,

we may write

$$\frac{r^2}{\alpha_r} \frac{d^2 \alpha_r}{dr^2} = n(n+3) + 2, \quad (\text{A5})$$

$$-\frac{1-\mu^2}{\alpha_\theta} \frac{d^2 \alpha_\theta}{d\mu^2} = n(n+3) + 2. \quad (\text{A6})$$

It is easy to show that the radial part  $\alpha_r$  has a solution of the form

$$\alpha_r = C_l r^l, \quad (\text{A7})$$

where  $C_l$  is a constant, and integer  $l$  must satisfy  $l(l-1) = n(n+3) + 2$ . Solving this quadratic, we see that  $l$  can take on the value  $n+2$  or  $-(n+1)$ .  $l = n+2$  corresponds to a positive power of  $r$  and a potential which monotonically increases with distance from the planet — this is not physical. Therefore, we choose  $l = -(n+1)$  for the radial part of the function.

To solve for the angular function  $\alpha_\theta$  we require knowledge of the Jacobi polynomials. The particular strand of these polynomials which are of use to us here are denoted  $P_n^{1,1}(\mu)$  ( $n$  is an integer  $\geq 0$  so we can associate a polynomial with each choice of  $n$  in equations A5 and A6). The useful property of the polynomials  $P_n^{1,1}(\mu)$  is that the functions  $(1-\mu^2)P_n^{1,1}(\mu)$  are actually solutions of the Eq. (A6). For a given choice of  $n$  our homogeneous solution would thus be

$$\alpha_H(r, \mu) = \alpha_r \alpha_\theta = C_n r^{-(n+1)} (1-\mu^2) P_n^{1,1}(\mu). \quad (\text{A8})$$

Since Eq. (A4) is linear in  $(\alpha_r, \alpha_\theta)$ , it follows that any linear combination of solutions of the above form is also a homogeneous solution. Without loss of generality, the complete homogeneous solution is thus

$$\alpha_H(r, \mu) = (1-\mu^2) \sum_{n=0}^{\infty} C_n r^{-(n+1)} P_n^{1,1}(\mu). \quad (\text{A9})$$

We have now found solutions for the *homogeneous* (source-free) version of Caudal's equation. But how do we use these to obtain a solution for the full differential Eq. (3) which contains the source function  $g$ ? We try a general solution obtained by multiplying each term in the series of the homogeneous solution by a purely radial function  $f_n(r)$ . This trial function thus takes the form

$$\alpha(r, \mu) = (1-\mu^2) \sum_{n=0}^{\infty} f_n(r) r^{-(n+1)} P_n^{1,1}(\mu), \quad (\text{A10})$$

where we have absorbed the constant  $C_n$  into the definition of  $f_n(r)$ . Now if we use this trial solution in the left-hand side of Eq. (3), we obtain

$$(1-\mu^2) \sum_{n=0}^{\infty} \left( \frac{d^2 f_n}{dr^2} - \frac{2(n+1)}{r} \frac{df_n}{dr} \right) r^{-(n+1)} P_n^{1,1}(\mu) = g(r, \mu, \alpha_{i-1}). \quad (\text{A11})$$

Here we have introduced the symbol  $i$  to emphasise that solving this equation is part of an iterative process where the current solution  $\alpha_i$  is obtained from the previous one  $\alpha_{i-1}$ . Although the left-hand side of our equation retains the form of a series summation in the Jacobi polynomials, we can't progress much further without addressing the right-hand side. This is where the Jacobi polynomials again prove useful. They are an orthogonal, complete set of functions, which means that *any* function of  $\mu$  can be expressed as a series expansion using Jacobi polynomials. Applying this to our function  $g$  for an arbitrary value of radial distance  $r$ , we

can decompose the angular dependence of  $g$  into a sum over the polynomials as follows

$$g(r, \mu, \alpha_{i-1}) = (1-\mu^2) \sum_{n=0}^{\infty} g_n(r) P_n^{1,1}(\mu), \quad (\text{A12})$$

with the expansion coefficients defined by the orthogonality condition

$$g_n(r) = \frac{1}{h_n} \int_{-1}^1 g(r, \mu) P_n^{1,1}(\mu) d\mu, \quad (\text{A13})$$

$$h_n = \int_{-1}^1 (1-\mu^2) (P_n^{1,1}(\mu))^2 d\mu. \quad (\text{A14})$$

We can now make use of the orthogonality of the polynomials to equate the  $n$ -th terms of Eqs. (A11–A12). This gives

$$\left( \frac{d^2 f_n}{dr^2} - \frac{2(n+1)}{r} \frac{df_n}{dr} \right) r^{-(n+1)} = -g_n(r), \quad (\text{A15})$$

or equivalently (multiplying both sides by  $r^{-(n+1)}$ )

$$r^{-2(n+1)} \frac{d^2 f_n}{dr^2} - 2(n+1) r^{-(2n+3)} \frac{df_n}{dr} = -r^{-(n+1)} g_n(r). \quad (\text{A16})$$

We see that the left-hand side can be expressed as the derivative of a product

$$\frac{d}{dr} \left( r^{-2(n+1)} f'_n \right) = -r^{-(n+1)} g_n(r). \quad (\text{A17})$$

The left-hand side of this equation is readily integrable. But we see that the general solution for the  $f_n(r)$  functions will involve integrals of the source function  $g$ . What this means in practice is that we have to numerically integrate some kind of empirical or other function which is a fit to observed plasma distributions. Caudal (1986)'s work shows that the source function includes quantities such as plasma pressure, plasma temperature (assumed isotropic) and mean ion mass. We now finalise the integration towards a final solution. We start with Eq. (A17) and rename the dummy variable for radial distance to  $u$

$$\frac{d}{du} \left( u^{-2(n+1)} f'_n \right) = -u^{-(n+1)} g_n(u). \quad (\text{A18})$$

We now integrate both sides over the range  $r_c$  to  $r$ .  $r_c$  is an inner boundary, similar to the planetary radius, which encloses the region where the field is purely a dipole field i.e. purely due to the planet's internal source. We adopt the boundary condition that  $f_n = 0$  at  $u = r_c$  (i.e. the contributions to the potential from the plasma source disappear at the inner boundary) and  $f'_n = f'_c$  at  $u = r_c$  (there is a 'jump' in the potential gradient at the inner boundary  $u = r_c$  supported by currents flowing on that surface). Performing this integration between  $u = r_c$  and  $u = r$  gives us

$$f'_n = r^{2(n+1)} \left( f'_c r_c^{-2(n+1)} - G(r) \right), \quad (\text{A19})$$

where  $G(r)$  denotes the function

$$G(r) = \int_{r_c}^r u^{-(n+1)} g_n(u) du, \quad (\text{A20})$$

$$\frac{dG}{dr} = r^{-(n+1)} g_n(r). \quad (\text{A21})$$

If we integrate Eq. (A18) between the limits  $u = r_c$  and  $u = \infty$  we obtain the useful identity

$$f'_c r_c^{-2(n+1)} = G(\infty). \quad (\text{A22})$$

We can now integrate Eq. (A19) by parts using the boundary conditions  $G(r_c) = 0$  and  $f_n(r_c) = 0$  to get

$$f_n(r) = f'_c r_c^{-2(n+1)} \int_{r_c}^r u^{2(n+1)} du - \frac{1}{2n+3} \left( r^{2n+3} G(r) - \int_{r_c}^r u^{n+2} g_n(u) du \right). \quad (\text{A23})$$

If we now make use of Eq. (A22) to eliminate the unknown  $f'_c$ , and perform the first integral, we obtain

$$f_n(r) = \frac{1}{2n+3} (r^{2n+3} - r_c^{2n+3}) G(\infty) - \frac{1}{2n+3} \left( r^{2n+3} G(r) - \int_{r_c}^r u^{n+2} g_n(u) du \right). \quad (\text{A24})$$

Since, by definition  $G(\infty) - G(r) = \int_r^\infty g_n u^{-(n+1)} du$ , we can combine the two terms with factor  $r^{2n+3}$  and multiply both sides by  $r^{-(n+1)}$  to get the following form for the full radial part of the solution

$$f_n(r) r^{-(n+1)} = \frac{1}{2n+3} \left[ r^{n+2} \int_r^\infty u^{-(n+1)} g_n(u) du + r^{-(n+1)} \left( \int_{r_c}^r u^{n+2} g_n(u) du - r_c^{2n+3} \int_{r_c}^\infty u^{-(n+1)} g_n(u) du \right) \right]. \quad (\text{A25})$$

We have written the solution in this form so that it reflects the full radial part of the solution given in Eq. (A10). This radial part of the full solution agrees with that given by Caudal (1986) and Lackner (1970). Their work shows that the integral multiplied by a factor  $r_c^{2n+3}$  comes about by assuming a boundary condition for  $f'_n$  different from zero. However, Caudal points out that this extra integral corresponds to surface currents at  $r = r_c$  and makes negligible contribution to the solution beyond a few planetary radii. In fact for his final calculations he omits it and relies on a more detailed internal field model. For the work described in this paper, we use a simple centred dipole representation of Saturn's field, with equatorial field strength as given in Table 1.

The final solution consists of the homogeneous part (assumed to be the dipole or other appropriate potential) added to the particular solution (non-zero source) whose radial and angular parts we have derived above. For completeness, we now give here the final solution for the magnetodisc potential

$$\alpha(r, \mu) = \frac{1 - \mu^2}{r} + (1 - \mu^2) \sum_{n=0}^{\infty} \frac{P_n^{1,1}(\mu)}{2n+3} \left[ r^{n+2} \int_r^\infty g_n(u) u^{-(n+1)} du + r^{-(n+1)} \left( \int_{r_c}^r u^{n+2} g_n(u) du - r_c^{2n+3} \int_{r_c}^\infty u^{-(n+1)} g_n(u) du \right) \right]. \quad (\text{A26})$$

This represents, in practice, a cumbersome calculation. The number of terms required in the polynomial series depends on how accurate a representation is needed for the source function (whether empirical or theoretical). Source functions characterised by larger angular scales require fewer polynomials in the expansion. For the work described in this paper, we used polynomial expansion up to degree  $n = 30$ . The corresponding latitudinal resolution captured by the polynomial of this degree is  $\sim 2.2^\circ$ , corresponding to typical vertical resolutions at the equator in the range 0.2–1 R<sub>S</sub>. To obtain

**Table B1.** Scaling values between variables in physical units and their dimensionless counterparts for both planets.

Dimension	Definition	Units	Saturn	Jupiter
<i>Primary scales</i>				
Length	$a$	km	60280	71492
Magnetic Field	$B_0$	nT	21160	428000
<i>Derived scales</i>				
Volume	$a^3$	km <sup>3</sup>	$2 \cdot 10^{14}$	$4 \cdot 10^{14}$
Magnetic Flux	$B_0 a^2$	GWb	77	2187
Current density	$B_0 / (a \mu_0)$	nA m <sup>-2</sup>	280	4800
Pressure	$B_0^2 / \mu_0$	Pa	0.00036	0.146
Energy density	$B_0^2 / \mu_0$	J m <sup>-3</sup>	0.00036	0.146
Hot plasma index $K_h$	$B_0 a / \mu_0$	Pa m T <sup>-1</sup>	$10^9$	$2 \cdot 10^{10}$

final model outputs, we stopped iteration when the maximum relative difference in the solution for the magnetic potential  $\alpha$  between consecutive iterations became less than 0.5 percent.

## APPENDIX B: SCALING OF PHYSICAL QUANTITIES

Table B1 presents a summary of the scaling values for all dimensionless quantities.